



1 **ISWFoam: A numerical model for internal solitary wave** 2 **simulation in continuously stratified fluids**

3 Jingyuan Li¹, Qinghe Zhang¹, Tongqing Chen¹

4 ¹State Key Laboratory of Hydraulic Engineering Simulation and Safety, Tianjin University, Tianjin
5 300072, China

6 *Correspondence to:* Qinghe Zhang (qhzhang@tju.edu.cn)

7 **Abstract.** A numerical model, ISWFoam, for simulating internal solitary waves (ISWs) in continuously
8 stratified, incompressible, viscous fluids is developed based on a fully three-dimensional (3D) Navier-
9 Stokes equation using the open source code OpenFOAM. This model combines the density transport
10 equation with the Reynolds-averaged Navier-Stokes equation with the Coriolis force, and the model
11 discrete equation adopts the finite volume method. The $k-\omega$ SST turbulence model has also been modified
12 accordingly to the variable density field. ISWFoam provides two initial wave generation methods to
13 generate an ISW in continuously stratified fluids, including solving the weakly nonlinear models of the
14 extended Korteweg–de Vries (eKdV) equation and the fully nonlinear models of the Dureuil-Jacotin-
15 Long (DJL) equation. Grid independence tests for ISWFoam are performed, considering the accuracy
16 and computing efficiency, the appropriate grid size of the ISW simulation is recommended to be one-
17 one hundred and fiftieth of the characteristic length and one-twenty fifth of the ISW amplitude. Model
18 verifications are conducted through comparisons between the simulated and experimental data for ISW
19 propagation examples over a flat bottom section, including laboratory scale and actual ocean scale, a
20 submerged triangular ridge, a Gaussian ridge and slope. The laboratory test results, including the ISW
21 profile, wave breaking location, ISW arrival time, and the spatial and temporal changes in the mixture
22 region, are well reproduced by ISWFoam. The ISWFoam model with unstructured grids and local mesh
23 refinement can accurately simulate the generation and evolution of ISWs, the ISW breaking phenomenon
24 and the interaction between ISWs and complex structures and topography.

25 **Key words.** OpenFoam, Internal solitary wave tank, Stratified fluid, the DJL equation, Grid
26 independence.

27 **1. Introduction**

28 Internal solitary waves (ISWs) are commonly observed in oceans, particularly on continental shelf



29 regions, due to strong tidal current flows over large topographic features (Huthnance, 1981), such as in
30 the northern South China Sea (Alford et al., 2010; Alford et al., 2015; Cai et al., 2012). ISWs play an
31 important role in both conveying nutrients from the deep ocean to shallower layers and promoting
32 biological growth (Sandstrom et al., 1984). Additionally, ISWs are a potential threat to the ocean
33 structures of resource exploration, exploitation, and submarine navigation vehicles (Alford et al., 2010;
34 Osborne et al., 1980). A considerable number of studies, which include field measurements, remote
35 sensing, experiments, theoretical analysis and numerical simulations, have been carried out due to the
36 significance of ISWs (Vlasenko et al., 2005; Apel et al., 2006; Alford et al., 2011; Guo et al., 2014).

37 For numerically simulated ISWs, many models have been adopted, including the Euler equation,
38 the inviscid/viscid incompressible Boussinesq model, the hydrostatic model, the non-hydrostatic model,
39 and the VOF based two-phase flow model. Among these models, the representative hydrostatic models
40 include the Naval Research Laboratory Ocean Nowcast/Forecast System (ONFS) (Ko et al., 2008), the
41 Regional Hallberg Isopycnal Tide Mode (RHIMT) (Hallberg and Rhines, 1996; Hallberg, 1997), and the
42 Ostrovsky-Hunter model. The representative non-hydrostatic models include the Bergen Ocean Model
43 (BOM), the nonhydrostatic Regional Ocean Modeling System model (ROMS), the Stanford
44 Unstructured Nonhydrostatic Terrain-following Adaptive Navier-Stokes Simulator (SUNTANS), and the
45 Massachusetts Institute of Technology general circulation model (MITgcm). For example, Zhang et al
46 (2012) established a variable water depth internal wave numerical model in a continuously stratified fluid
47 system based on the Euler equation. Xu and Stastna (2020) used the viscid incompressible Boussinesq
48 model to study cross-boundary-layer transport (Boegman and Stastna, 2019) by the fissioning process of
49 shoaling ISWs. Lamb (1994) established a non-hydrostatic model, using a second-order projection
50 method developed by Bell and Marcus (1992), which is used for internal wave research including
51 boundary layer instability (Aghsaee et al., 2012), reflection (Lamb, 2009), and the interaction of the tides
52 with the topography (Lamb, 2007; Aghsaee et al., 2010). Diamessis (2005) developed a spectral
53 multidomain penalty method model and correctly reproduced the characteristic vorticity and internal
54 wave structure. Subich et al (2013) developed a spectral collocation method for the solution of the
55 Navier–Stokes equations under the Boussinesq approximation, and simulated the internal wave in
56 continuously stratified fluid. Smedstad et al (2003) employed the ONFS model to establish a global ocean
57 real-time forecasting system with an operational eddy resolution of $1/16^\circ$, which effectively tracks ocean



58 eddies, ocean currents and ocean fronts. [Simmons et al \(2004\)](#) employed the RHIMT model to carry out
59 a global numerical simulation of tidal currents, and analyzed the whole process of the conversion rate of
60 barotropic waves into baroclinic waves. [Thiem \(2011\)](#) used the Bergen Ocean Model to explore the
61 bottom boundary layer flow caused by waves beneath a propagating ISW in a two-fluid system. [Li and
62 Farmer \(2011\)](#) employed the Ostrovsky-Hunter model to study the nonlinear evolution of a
63 monochromatic internal wave. [Buijsman et al \(2010\)](#) employed ROMS model to study the asymmetry in
64 solitons to the east and west of Luzon Strait. [Zhang et al \(2011\)](#) used the nonhydrostatic SUNTANS
65 model ([Fringer et al., 2006](#)) to study the dynamics of A wave and B wave formation. [Rayson et al \(2018\)](#)
66 used the modified SUNTANS model to study the internal waves around Scott Reef and provided the
67 generation process of internal lee waves. [Vlasenko et al \(2010\)](#) employed the MITgcm model to
68 investigate the baroclinic tidal energy conversion in the area west of the Luzon Strait.

69 In summary, for continuously stratified fluids in complex ocean environments, numerical simulation
70 has become a leading method for ISW investigations. However, there are presently few versatile
71 numerical models with share code that can accurately simulate the ISW flow around complex topography
72 and submarine navigation vehicles in continuously stratified fluids. Therefore, the main objective of this
73 paper is to develop a solver, referred to as ISWFoam with a modified $k-\omega$ SST model that considers the
74 variable density field, which simulates the ISW in continuous density stratification, incompressible and
75 viscous fluids using the finite volume method with unstructured grids based on a fully three-dimensional
76 (3D) Navier-Stokes equation using the OpenFOAM library.

77 Notably, the open source field operation and manipulation code OpenFOAM®, as an object-
78 oriented C++ open source library that can be used to build a variety of solvers for computational fluid
79 problems based on the finite volume method, is becoming increasingly popular in the computational fluid
80 research community. At present, the official version of OpenFOAM® does not have a solver or boundary
81 conditions for solving the ISW in continuously stratified fluids. Although some researchers simulate
82 ISWs by modifying the OpenFOAM® code, most of these studies are based on a two-fluid system
83 without considering continuous stratification in density, such as [Meng and Zhang \(2016\)](#) and [Li et al
84 \(2017\)](#). Though recent work by [Ding et al \(2020\)](#) and [Li et al \(2021\)](#) considered continuous stratification
85 in density, the wave generation method is essential for a two-layer system. To extensively use of the
86 numerical model of ISWs as a tool in the future, we will develop ISWFoam to simulate the ISW in



87 continuously stratified, incompressible and viscous fluids based on the OpenFOAM library. The
88 turbulence model will consider the variable density field. In addition, ISWfoam will provide two initial
89 methods to generate an ISW in continuously stratified fluids, including solving the weakly nonlinear
90 models of the extended Korteweg-de Vries (eKdV) equation and the fully nonlinear models of the
91 Dubreil-Jacotin-Long (DJL) equation. This approach renders the numerical model suitable for the
92 simulation of ISW flows in complex geometries and topographies.

93 The outline of the paper is described as follows. First, in Section 2, the governing equations for a
94 continuously stratified fluid are presented, and discrete forms of these equations are derived. Then, grid
95 independence tests of the developed ISWfoam model are described in Section 3. Subsequently, in
96 Section 4, a series of test cases are presented to verify the model. Finally, the conclusions are drawn in
97 Section 5.

98 2. ISWfoam: A three-dimensional numerical solver for ISWs in a continuously stratified fluid

99 2.1 Governing equations

100 We present an ISW numerical model by solving the motion of a three-dimensional, viscous,
101 incompressible fluid with the Boussinesq approximation and rigid lid hypothesis. The governing
102 equations of the model are

$$103 \quad \nabla \cdot \mathbf{U} = 0, \quad (1)$$

$$104 \quad \frac{\partial \mathbf{U}}{\partial t} + (\mathbf{U} \cdot \nabla) \mathbf{U} - \nabla \cdot (v_{eff} \nabla \mathbf{U}) = \mathbf{Q} \quad \mathbf{Q} = \frac{1}{\rho_0} \left(-\nabla p_{rgh} - \mathbf{g} \cdot \mathbf{X} \nabla \rho - \Omega \mathbf{e}_3 \right), \quad (2)$$

$$105 \quad \frac{\partial \rho}{\partial t} + (\mathbf{U} \cdot \nabla) \rho = \nabla \cdot (k \nabla \rho), \quad (3)$$

106 where $\mathbf{U} = (u_i, u_j, u_k)$ is the velocity vector, t is time, ∇ is the gradient operator, \mathbf{Q} is the source term,
107 ρ_0 is the reference density, ρ is the density field, p_{rgh} is a modified pressure field, \mathbf{g} is the gravitational
108 acceleration vector, and \mathbf{X} is the position vector. v_{eff} is the effective kinematic viscosity defined as $v_{eff} =$
109 μ_{eff} / ρ_0 , where μ_{eff} is the effective dynamic viscosity including the molecular viscosity (μ) and turbulent
110 viscosity (μ_t). k is the diffusion coefficient, and its value is the same as the effective dynamic
111 viscosity (μ_{eff}). Ω is the Coriolis parameter, which is the twice the speed of rotation around the vertical
112 unit vector $\mathbf{e}_3 = (0, 0, 1)$. ISWfoam uses a modified pressure p_{rgh} instead of a total pressure p , and their
113 relationship is given by



$$114 \quad p_{\text{rgh}} = p - \rho \mathbf{g} \cdot \mathbf{X}, \quad \nabla p_{\text{rgh}} = \nabla p - \rho \mathbf{g} - \mathbf{g} \cdot \mathbf{X} \nabla \rho, \quad (4)$$

115 To close the above equations, the turbulence model needs to be employed. The two-equation k - ε
 116 model is widely used as an effective turbulence model, but it cannot capture the proper behaviour of
 117 turbulent boundary layers up to separation due to adverse pressure gradients (Wilcox, 1993). For the
 118 above boundary layers separation problem, Bardina et al. (1997) and Menter et al. (2003) suggested the
 119 use of the k - ω SST model to obtain substantially more accurate results. Therefore, the turbulence model
 120 used in this paper is the k - ω SST model. Notably that in OpenFOAM, the incompressible version for
 121 turbulence models does not consider the variable density field, and instead, it treats the density as a
 122 constant, such as the k - ω SST model

$$123 \quad \frac{\partial k}{\partial t} + \nabla \cdot (\mathbf{U}k) = \nabla \cdot \left[(v_{\text{eff}} + \sigma_k v_t) \nabla k \right] + P_k^* - \beta^* \omega k \quad (5)$$

$$124 \quad \frac{\partial \omega}{\partial t} + \nabla \cdot (\mathbf{U}\omega) = \nabla \cdot \left[(v_{\text{eff}} + \sigma_\omega v_t) \nabla \omega \right] + C_\gamma \frac{\omega}{k} P_k - C_\beta \omega^2 + 2(1 - F_1) \frac{\sigma_{\omega 2}}{\omega} \nabla k \cdot \nabla \omega \quad (6)$$

$$125 \quad P_k^* = \min(P_k, c_1 C_\mu k \omega) \quad (7)$$

$$126 \quad v_t = \frac{a_1 k}{\max(a_1 \omega, \sqrt{2} S_i F_2)} \quad (8)$$

127 where k is the turbulent kinetic energy, ω is the specific dissipation rate, P_k is the production term of k ,
 128 $P_k = \tau^R : \nabla \mathbf{U}$, P_k^* is related to the production term of turbulence kinetic energy P_k in the k equation, v_t
 129 is the turbulent kinematic viscosity, S_i is the mean rate of the flow strain, $S_i = 0.5(\nabla \mathbf{U} + \nabla \mathbf{U}^T)$, the model
 130 constants are assigned the values $\beta^* = 0.09$, $a_1 = 0.31$, $c_1 = 10$ and $C_\mu = 0.09$, F_1 and F_2 are blending
 131 functions, the value of σ_k , σ_ω , C_γ and C_β are blended using the equation $\Phi = F_1 \Phi_1 + (1 - F_1) \Phi_2$ in which
 132 Φ_1 and Φ_2 are given in Table 1.

133 Table 1 Default values for Φ_1 and Φ_2

Φ	σ_k	σ_ω	C_β	C_γ
Φ_1	0.85	0.5	0.075	5/9
Φ_2	1.0	0.856	0.0828	0.44

134

135 Considering the variable density field during the solution process, it is necessary to consider the
 136 change in the density field in the turbulence model. Therefore, we modify the turbulence model to
 137 consider the change in density, and finally a modified k - ω SST model that considers the change in density
 138 is used to close the equation



$$139 \quad \frac{\partial \rho k}{\partial t} + \nabla \cdot (\rho \mathbf{U} k) = \nabla \cdot [\rho (v_{\text{Eff}} + \sigma_k v_t) \nabla k] + \rho P_k^* - \rho \beta^* \omega k \quad (9)$$

$$140 \quad \frac{\partial \rho \omega}{\partial t} + \nabla \cdot (\rho \mathbf{U} \omega) = \nabla \cdot [\rho (v_{\text{Eff}} + \sigma_\omega v_t) \nabla \omega] + C_\gamma \frac{\omega}{k} P_k - C_\beta \rho \omega^2 + 2(1 - F_1) \rho \frac{\sigma_\omega^2}{\omega} \nabla k \cdot \nabla \omega \quad (10)$$

141

142 2.2 Numerical discretization

143 The governing equations are numerically discretized using the finite volume method based on the
 144 C++ open source library of OpenFOAM. The finite volume method requires that Eqs. (2) and (3) are
 145 satisfied over the control volume V_P around point P in integral form:

$$146 \quad \int_{V_P} \int_{\Delta t} \left[\frac{\partial \mathbf{U}}{\partial t} + (\mathbf{U} \cdot \nabla) \mathbf{U} - \nabla \cdot (v_{\text{Eff}} \nabla \mathbf{U}) \right] dV dt = \int_{V_P} \int_{\Delta t} Q dV dt, \quad (11)$$

$$147 \quad \int_{V_P} \int_{\Delta t} \left[\frac{\partial \rho}{\partial t} + (\mathbf{U} \cdot \nabla) \rho - \nabla \cdot (k \nabla \rho) \right] dV dt = 0, \quad (12)$$

148 The momentum equation in ISWFOam is solved by constructing a predicted velocity field and then
 149 using the Pressure Implicit with Splitting of Operators (PISO) algorithm (Issa, 1986) to modify it. n is
 150 defined to represent the current moment. The PISO iteration process is marked as m ; when m is equal to
 151 zero, it represents the initial moment (t^n).

152 First, only the temporal, convection and diffusion terms appear in the discrete version of the
 153 equation momentum, and the other terms are ignored. After this operation, we obtain an explicit
 154 expression for the predicted velocity field \mathbf{U}_P^r , namely,

$$155 \quad \frac{\mathbf{U}_P^r - \mathbf{U}_P^n}{\Delta t} V_P + \sum_{f \in \partial V_P} (\phi_f^n \mathbf{U}_f^r) - \sum_{f \in \partial V_P} v_{\text{Eff}} \nabla \mathbf{U}_f^r \cdot \mathbf{S}_f = 0, \quad (13)$$

156 where P represents the centre of the grid cell, $\phi_f^n = \mathbf{U}_f^n \cdot \mathbf{S}_f$ is the volume flux at the initial time n and
 157 \mathbf{S}_f is the face vector.

158 The solution process requires the velocity on the surface f . Assuming the variation in \mathbf{U}_f^r between
 159 the centre P of the grid and the centre N of the adjacent grid, the face values are calculated using a mixture
 160 method (blended differencing) of the central scheme (central differencing) and the upwind scheme
 161 (upwind differencing) as follows (Jasak, 1996):

$$162 \quad \mathbf{U}_f = (1 - \lambda_u) (\mathbf{U}_f)_{UD} + \lambda_u (\mathbf{U}_f)_{CD} \quad (14)$$

163 where



$$164 \quad (\mathbf{U}_f)_{UD} = \begin{cases} \mathbf{U}_P \text{ for } \phi_f \geq 0, \\ \mathbf{U}_N \text{ for } \phi_f < 0, \end{cases} \quad \text{and} \quad (\mathbf{U}_f)_{CD} = \frac{\mathbf{U}_P + \mathbf{U}_N}{2} \quad (15)$$

165 where N represents the centre of the adjacent grid cells, $\phi_f = \mathbf{U}_f \cdot \mathbf{S}_f$ is volume flux. The limiter λ_U
 166 can be selected from several alternatives (OpenFOAM, 2019), including linear, QUICK, vanLeer, etc. In
 167 the following derivation process, the vanLeer scheme was used to calculate the velocity of the face centre

$$168 \quad \mathbf{U}_f = \frac{1}{2}(\mathbf{U}_P + \mathbf{U}_N) + \frac{1}{2}[\psi(\phi_f)(1 - \lambda_U)](\mathbf{U}_P - \mathbf{U}_N), \quad (16)$$

169 where $\psi(\phi_f)$ is a step function defined by

$$170 \quad \psi(\phi_f) = \begin{cases} 1 \text{ for } \phi_f \geq 0, \\ -1 \text{ for } \phi_f < 0, \end{cases} \quad (17)$$

171 Inserting Eq. (16) into Eq. (13) yields

$$172 \quad A_P \mathbf{U}_P^r = \sum_{f \in \partial V_P} A_N \mathbf{U}_P^m + \frac{\mathbf{U}_P^n}{\Delta t} = H(\mathbf{U}^m) \quad (18)$$

173 After some manipulation, the quantities A_P and A_N are given as

$$174 \quad A_P = \left\{ \frac{V_P}{\Delta t} + \sum_{f \in \partial V_P} \frac{\phi_f^n}{2} [1 + \psi(\phi_f)(1 - \lambda_U)] + \sum_{f \in \partial V_P} v_{Eff,f} \frac{|\mathbf{S}_f|}{|d|} \right\} \frac{1}{V_P} \quad (19)$$

$$175 \quad A_N = \left\{ -\frac{\phi_f^n}{2} [1 - \psi(\phi_f)(1 - \lambda_U)] + v_{Eff,f} \frac{|\mathbf{S}_f|}{|d|} \right\} \frac{1}{V_P} \quad (20)$$

176 Including the effect of gravity and the Coriolis force in Eq. (18)

$$177 \quad \mathbf{U}_P^r = \frac{H(\mathbf{U}^m)}{A_P} - \frac{(\mathbf{g} \cdot \mathbf{X} \nabla \rho / \rho_0)^n}{A_P} - \frac{(\Omega \mathbf{e}_3)^n}{A_P}, \quad (21)$$

178 Notably, that when m is equal to zero, it represents the initial moment n , and the value of the initial
 179 moment is known. Therefore, we obtain the predicted velocity field \mathbf{U}_P^r in the first iteration. We define

180 the surface gradient operator $(\nabla_{\frac{1}{f}})$, and the type of gradient operator acting on \mathbf{U} is

181 $\nabla_{\frac{1}{f}} \mathbf{U} = (\mathbf{U}_N^m - \mathbf{U}_P^m) / |d|$, which represents the distance from the centre of the grid N to P . Similarly,

182 the surface gradient operator $(\nabla_{\frac{1}{f}})$ acting on scalar γ is $\nabla_{\frac{1}{f}} \lambda = (\lambda_N^m - \lambda_P^m) / |d|$. The associated flux

183 $(\phi_f = \mathbf{U}_f \cdot \mathbf{S}_f)$ is achieved by executing an inner product with a surface vector (\mathbf{S}_f) on the left and right

184 parts of Eq. (21), giving



$$\phi_f^r = \left(\frac{H(\mathbf{U}^m)}{A_p} \right)_f \cdot \mathbf{S}_f - \left(\left(\frac{1}{A_p} \right)_f (\mathbf{g} \cdot \mathbf{X})_f^n \left(\frac{1}{\rho_0} \nabla_{\perp} p_{-rgh} \right)_f^n |\mathbf{S}_f| \right) - \left(\frac{(\Omega e_3)^n}{A_p} \right)_f \cdot \mathbf{S}_f, \quad (22)$$

Eq. (22) completed the flux calculation without considering the influence of the pressure term. The pressure contribution in terms of a flux can be expressed as

$$\left(\frac{-\nabla p_{-rgh}}{\rho_0 A_p} \right)_f \cdot \mathbf{S}_f = \left(\frac{-1}{A_p} \right)_f \left(\frac{1}{\rho_0} \nabla_{\perp} p_{-rgh}^{m+1} \right)_f |\mathbf{S}_f|, \quad (23)$$

Then, Eq. (23) is now added to Eq. (22) to yield

$$\phi_f^{m+1} = \left(\frac{H(\mathbf{U}^m)}{A_p} \right)_f \cdot \mathbf{S}_f - \left(\left(\frac{1}{A_p} \right)_f (\mathbf{g} \cdot \mathbf{X})_f^n \left(\frac{1}{\rho_0} \nabla_{\perp} p_{-rgh} \right)_f^n |\mathbf{S}_f| \right) - \left(\frac{(\Omega e_3)^n}{A_p} \right)_f \cdot \mathbf{S}_f - \left(\frac{1}{A_p} \right)_f \left(\frac{1}{\rho_0} \nabla_{\perp} p_{-rgh}^{m+1} \right)_f |\mathbf{S}_f| \quad (24)$$

Combined with Eq. (22), Eq. (24) is simplified and rewritten as

$$\phi_f^{m+1} = \phi_f^r - \left(\frac{1}{A_p} \right)_f \left(\frac{1}{\rho_0} \nabla_{\perp} p_{-rgh}^{m+1} \right)_f |\mathbf{S}_f| \quad (25)$$

Using conservation of mass, we solve the pressure field p_{-rgh}^{m+1} , which results in

$$\sum_{f \in \partial V_p} \left(\frac{1}{A_p} \right)_f \left(\frac{1}{\rho_0} \nabla_{\perp} p_{-rgh}^{m+1} \right)_f |\mathbf{S}_f| = \sum_{f \in \partial V_p} \phi_f^r \quad (26)$$

The preconditioned conjugate gradient method is used to solve the linear system constructed by Eq. (26) (OpenFOAM, 2019). After p_{-rgh}^{m+1} is obtained using Eq. (26), we calculate the volume flux using Eq. (25) for each face. The cell-centred velocity fields \mathbf{U}_p^{m+1} are calculated by reconstructing the face velocity flux using the following expression (Deshpande, 2012)

$$\mathbf{U}_p^{m+1} = \mathbf{U}_p^r + \left(\frac{1}{A_p} \right) \left(\sum_{f \in \partial V_p} \frac{\mathbf{S}_f \mathbf{S}_f}{|\mathbf{S}_f|} \right)^{-1} \cdot \left(\sum_{f \in \partial V_p} \left(\frac{\phi_f^{m+1} - (\mathbf{U}_p^r)_f \cdot \mathbf{S}_f}{(1/A_p)_f} \right) \frac{\mathbf{S}_f}{|\mathbf{S}_f|} \right) \quad (27)$$

Eq. (27) completes the velocity field calculation of the first iteration step in the PISO algorithm. By converting the identifier m to $m+1$, the next PISO iteration is completed and updating the velocity in Eq. (18) with the velocity \mathbf{U}_p^{m+1} calculated from Eq. (27), thereby updating p_{-rgh} , ϕ_f and \mathbf{U} . This procedure is performed M times to guarantee that the results of the velocity and pressure together conform to the continuity and momentum equations. Considering that PISO iteration levels require more than 1, but typically not more than 4 (OpenFOAM, 2019), we specify that the number of PISO iteration levels is 3



206 in the computations presented in this paper. After completing the three iterations, the converged values
207 are considered the result of the next time step ($n + 1$), namely,

$$208 \quad \phi_f^{n+1} = \phi_f^M, \quad \mathbf{U}_P^{n+1} = \mathbf{U}_P^M, \quad P_{-rgh}^{n+1} = P_{-rgh}^M, \quad (28)$$

209 We discretize the convection-diffusion equation of density (12) to obtain

$$210 \quad \frac{V_P}{\Delta t} (\rho_p^{n+1} - \rho_p^n) + \sum (\phi_f^{n+1} \rho_f^{n+1}) = \sum k \left[|\mathbf{S}_f| \frac{\rho_N^{n+1} - \rho_P^{n+1}}{|d|} \right], \quad (29)$$

211 At the end of the iteration procedure, we bring the results of the volume flux into Eq. (29) to
212 calculate the density field at the next time (ρ_p^{n+1}), thereby updating the density field for the next step
213 calculation ($\Delta t = t^{n+2} - t^{n+1}$).

214 2.3 Initialized field of ISW generation

215 ISW generation methods mainly include the gravity collapse mechanism, double push-pedals
216 method (Fu et al., 2008), velocity-inlet method (Gao et al., 2012), mass source method (Wang et al.,
217 2018), initialization method, and methods addressing the interaction between tidal current and
218 topography. For example, Hsieh et al (2014) investigated the flow evolution of a depression ISW
219 generated by the gravity collapse mechanism. Cheng et al (2020) studied the interaction between ISWs
220 and a cylinder using the gravity collapse mechanism. The initialization method involves solving the
221 internal solitary wave theory at the initial moment, such as the Korteweg-de Vries (KdV) equation
222 (Grimshaw et al., 2010), the modified KdV (mKdV) equation, the extended KdV (eKdV) equation, the
223 forced KdV equation, the Ostrovsky equation (Li and Farmer, 2011), the Miyata-Choi-Camassa (MCC)
224 model (Miyata 1985 and 1988; Choi and Camassa, 1999), and the Dubreil-Jacotin-Long (DJL) equation
225 (Long, 1953; Turkington, 1991; Brown and Christie, 1997; Dunphy et al., 2011), to obtain the wave
226 surface, velocity field. The method of an interacting between tidal current and terrain that stimulates
227 ISWs is adopted by many scholars, such as Farmer and Smith (1980), Lamb et al (1994), and Shaw et al
228 (2009).

229 In this paper, the method of initializing the field is selected to generate the ISWs. To increase the
230 application range of the ISWfoam model, two initialization methods are provided, including solving the
231 weakly nonlinear models of the eKdV equation (Helfrich and Melville, 2006) and the fully nonlinear
232 models of the DJL equation for continuously stratified fluids (Turkington, 1991; Dunphy et al, 2011).



233 The Dubreil-Jacotin-Long (DJL) equation is expressed as

$$234 \quad \nabla^2 \eta + \frac{N^2(z-\eta)}{c^2} \eta = 0, \quad \eta = 0 \quad \text{at} \quad z = 0, -H \quad (30)$$

$$\eta = 0 \quad \text{at} \quad |x| \rightarrow \infty$$

235 where η is the isopycnal displacement, H is the water depth, c is the propagation speed, N is the definition
 236 of the buoyancy frequency, and z is vertical position.

$$237 \quad N^2(z) = -g \frac{d\rho_0(z)}{dz}, \quad (31)$$

238 where $\rho_0(z)$ is the reference density, and g is the gravitational acceleration.

239 By solving the above DJL equation we can obtain η and c , and then through the relationship $\psi = \eta c$,
 240 where ψ is the stream function, we can obtain the wave-induced velocity field. We use the DJLES open
 241 source package provided by [Dunphy et al \(2011\)](#) to solve the DJL equations. Then we input the initial
 242 field calculated by DJLES into OpenFOAM to obtain the initial field required for OpenFOAM numerical
 243 simulation.

244 Another theory of ISWfoam model wave generation involves the weakly nonlinear models of the
 245 eKdV equation. Using the first order stream function for the DJL equation, we can obtain the well-known
 246 KdV equation and further obtain the eKdV equation. For the specific derivation, please refer to the paper
 247 by [Lamb and Yan \(1996\)](#). The eKdV equation ([Helfrich and Melville, 2006](#)) is

$$248 \quad \frac{\partial \zeta}{\partial t} + (c_0 + c_1 \zeta + c_3 \zeta^2) \frac{\partial \zeta}{\partial x} + c_2 \frac{\partial^3 \zeta}{\partial x^3} = 0, \quad (32)$$

$$249 \quad c_0^2 = \frac{gh_1 h_2 (\rho_2 - \rho_1)}{\rho_1 h_2 + \rho_2 h_1}, \quad (33)$$

$$250 \quad c_1 = -\frac{3c_0}{2} \frac{\rho_1 h_2^2 - \rho_2 h_1^2}{\rho_1 h_1 h_2^2 + \rho_2 h_1^2 h_2}, \quad (34)$$

$$251 \quad c_2 = \frac{c_0}{6} \frac{\rho_1 h_1^2 h_2 + \rho_2 h_1 h_2^2}{\rho_1 h_2 + \rho_2 h_1}, \quad (35)$$

$$252 \quad c_3 = \frac{3c_0}{h_1^2 h_2^2} \left[\frac{7}{8} \left(\frac{\rho_1 h_2^2 - \rho_2 h_1^2}{\rho_1 h_2 + \rho_2 h_1} \right)^2 - \frac{\rho_1 h_2^3 + \rho_2 h_1^3}{\rho_1 h_2 + \rho_2 h_1} \right], \quad (36)$$

253 where ζ is the isopycnal vertical displacement; h_1 and h_2 are the mean upper and lower layer depths,
 254 respectively; ρ_1 and ρ_2 are the fluid densities of the upper and lower layers, respectively. The theoretical



255 solution of Eq. (32) above is

$$256 \quad \zeta = \frac{a}{B + (1-B) \cosh^2 \left[\lambda_{\text{eKdV}} (x - c_{\text{eKdV}} t) \right]}, \quad (37)$$

$$257 \quad \lambda_{\text{eKdV}}^2 = \frac{a}{12c_2} \left(c_1 + \frac{1}{2} c_3 a \right), \quad (38)$$

$$258 \quad c_{\text{eKdV}} = c_0 + \frac{a}{3} \left(c_1 + \frac{1}{2} c_3 a \right), \quad (39)$$

$$259 \quad B = \frac{-ac_3}{2c_1 + ac_3}, \quad (40)$$

$$260 \quad u_1 = -c_{\text{eKdV}} \frac{\zeta}{h_1 - \zeta}, \quad u_2 = c_{\text{eKdV}} \frac{\zeta}{h_2 + \zeta}, \quad (41)$$

261 where a is the ISW amplitude, λ_{eKdV} is the wavelength, c_{eKdV} is the wave speed, B is an auxiliary parameter,
 262 and u_1 and u_2 are the speeds of the upper and lower layers of the fluid, respectively. The waveform and
 263 velocity field of the ISWs are solved at the initial moment by the developed function and then assigned
 264 to the calculation domain.

265 The vertical profile of the initial density is given by a hyperbolic tangent function profile (Aghsaee
 266 et al., 2010)

$$267 \quad \bar{\rho}(z) = \frac{\rho_1 + \rho_2}{2} - \frac{\rho_2 - \rho_1}{2} \tanh \left(\frac{z - z_{\text{pyc}}}{d_{\text{pyc}}} \right) \quad (42)$$

268 where z is the vertical position; ρ_1 and ρ_2 are the fluid densities of the upper and lower layers, respectively;
 269 z_{pyc} is the location of the centre of the pycnocline; and d_{pyc} is the thickness of the pycnocline. In this paper,
 270 unless otherwise specified, the form of the density profile adopts Eq. (42). The internal solitary wave
 271 surface is obtained by calculating the gradient of the density field, and the absolute value of the maximum
 272 value of the gradient represents the vertical position of the wave surface. Notably, the density profile of
 273 the actual ocean is not always hyperbolic, so our model provides a function for users to modify the
 274 density profile according to the actual situation.

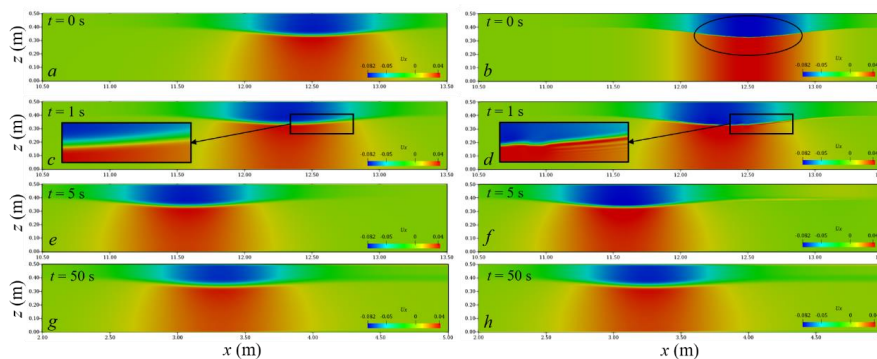
275 2.3.1 Comparison between the DJL equation and the eKdV equation

276 To compare the DJL equation and the eKdV equation, we set up a numerical simulation, which
 277 includes a tank that is 15 m long, 1 m wide and has a water depth of 0.5 m. The depths of the upper (h_1)
 278 and lower (h_2) layers are 0.1 m and 0.4 m, respectively, the densities of the upper and lower layers are
 279 1022 kg/m³ and 1028 kg/m³, respectively, the location of the centre of the pycnocline (z_{pyc}) is 0.4 m, the



280 pycnocline thickness (d_{pyc}) is 0.04 m vertically, the initial ISW amplitude (a) is 0.065 m and the location
 281 of the centre of ISW is 12.5m. The ISWs propagate from right to left. The measuring point P is set at a
 282 position 10m away from the initial ISW. The grid is uniform in the x -direction, y -direction and z -direction,
 283 and the sizes are $\Delta x = 1 \times 10^{-2}$ m, $\Delta y = 1 \times 10^{-2}$ m and $\Delta z = 1 \times 10^{-3}$ m, respectively. Slip boundary conditions
 284 are applied to the bottom and both sides, while cyclic boundary conditions are assigned to the inlet and
 285 outlet boundaries. The top boundary is a rigid lid. The boundary conditions related to the density field
 286 are no-flux boundary conditions.

287 Fig. 1 shows the comparison of the horizontal velocity component field when the DJL equation and
 288 the eKdV equation are used to generate ISWs. At the initial moment, the ISW generated by the eKdV
 289 equation is not as smooth as the ISW generated by the DJL equation, and the horizontal velocity at the
 290 interface area is discontinuous as shown in Fig. 1(a) and (b). With the propagation of ISWs, the ISWs
 291 generated by the DJL equation are always smooth at the interface area, and the velocity field is always
 292 continuous as shown in Fig. 1(a), (c), (e) and (g). Correspondingly, the ISW generated by the eKdV
 293 equation gradually produces a gradient in the vertical direction of the horizontal velocity in the interface
 294 area, thus, the interface area becomes smooth, and the velocity becomes continuous. Fig. 1(d) shows this
 295 evolution process, which is basically completed in 5s as shown in Fig. 1(f). At 50s, the difference between
 296 the horizontal velocity fields of the two equations is very small as shown in Fig. 1(g) and (h).

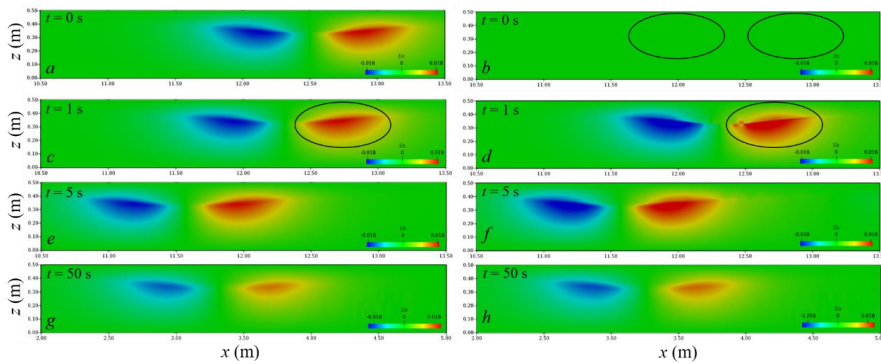


297
 298 Figure 1: Comparison chart of the horizontal velocity component field: DJL equation (left) and eKdV equation
 299 (right).

300 Fig. 2 shows the comparison of the vertical velocity component field when the DJL equation and
 301 the eKdV equation are used to generate ISWs. Since the theoretical solution of the eKdV equation only
 302 obtain the average horizontal velocity of the upper and lower layers of the fluid, there is no vertical
 303 velocity at the initial moment, as shown in Fig. 2(b). With the propagation of ISWs, the vertical velocity

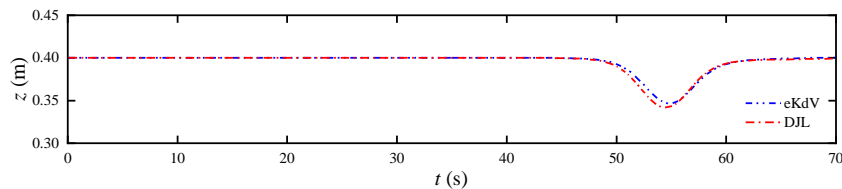


304 field will gradually be generated and finally stabilized, and the stable time occurs at 5s as shown in Fig.
 305 2(b), (d), (f) and (h). At 50s, the difference between the vertical velocity fields of the two equations is
 306 very small as shown in Fig. 2(g) and (h).



307
 308 Figure 2: Comparison chart of the vertical velocity component field: DJL equation (left) and eKdV equation
 309 (right).

310 The ISW propagates for 10 m, and the amplitudes of the ISWs generated by the DJL equation and
 311 the eKdV equation are reduced by 9.88% and 17.96%, respectively, as shown in Fig. 3. Overall, the
 312 reduction in energy leads to the attenuation of the amplitude of the ISW, which in turn reduces the wave
 313 speed. Except for the difference in initial fields, the grid sizes, time step, turbulence model, and other
 314 features are the same. Therefore, the initial stage of ISWs generated by the eKdV equation leads to
 315 excessive energy loss compared with those generated by the DJL equation. From the above analysis of
 316 the velocity field, we know that the method of initializing the field with the eKdV equation requires a
 317 period of movement before the jump of the velocity field develops into a field with continuous changes
 318 in velocity. In addition, the DJL equation, as a fully nonlinear model, can better reflect its superiority for
 319 internal waves with strong nonlinearity. Therefore, the wave generation of the subsequent numerical
 320 cases in this paper adopts the method of initializing the field with the DJL equation.



321
 322 Figure 3: Time series of the interface displacement. The probe was 10 m away from the initial ISW.



323 3. Grid independence of the ISW simulation

324 These grid independence tests were performed in the horizontal and vertical directions by applying
325 meshes of different sizes. The sizes of the mesh determined in this paper are calculated based on the
326 amplitude of the ISW and a characteristic length determined through the integration of the wave profile
327 (Michallet and Ivey, 1999)

$$328 \quad L = \frac{1}{a} \int_{-\infty}^{\infty} \zeta(x) dx \quad (43)$$

329 where ζ is the isopycnal vertical displacement and a is the ISW amplitude.

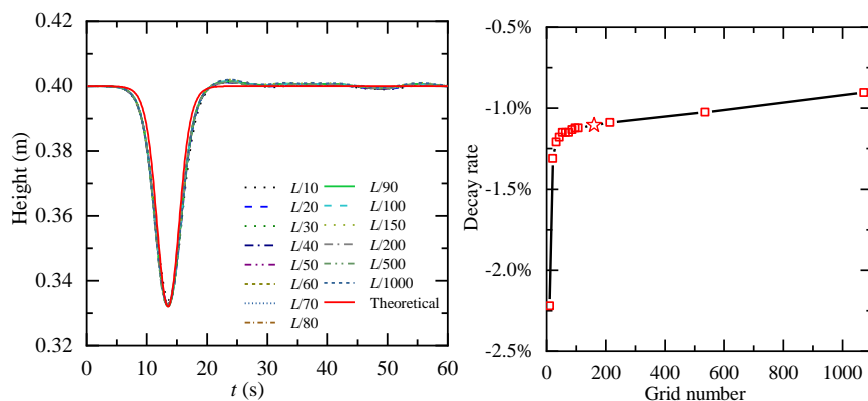
330 To determine the appropriate mesh size, the propagation of ISWs on flat bottoms is calculated, and
331 the numerical results are compared with the DJL theoretical solution. We set up a numerical simulation,
332 which includes a tank that is 50 m long, 0.5 m wide and has a water depth of 0.5 m. The depths of the
333 upper (h_1) and lower (h_2) layers are 0.1 m and 0.4 m, respectively, the densities of the upper and lower
334 layers are 1000 kg/m³ and 1030 kg/m³, respectively, the location of the centre of the pycnocline (z_{pyc}) is
335 0.4 m, and the pycnocline thickness (d_{pyc}) is 0.05 m vertically, the ISW amplitude (a) is 0.065 m. The
336 measuring point P is set at a position $10L$ away from the initial ISW. The sponge layer on both sides,
337 whose length is the double wave characteristic length, has been checked to properly dissipate the
338 reflected wave. Slip boundary conditions are applied to the bottom and both sides, while cyclic boundary
339 conditions are assigned to the inlet and outlet boundaries. The top boundary is a rigid lid. The boundary
340 conditions related to the density field are no-flux boundary conditions.

341 3.1 Grid independence in the horizontal direction

342 First, we analyse the grid independence in the horizontal direction, with a constant cell height of Δz
343 = $a/20$ m. Fig. 4 shows the results of the comparison of the waveform and decay rate in the horizontal
344 direction at probe P1 with the ISWfoam using a wide range of grid configurations. The results show a
345 negligible difference in the waveform when the mesh size is less than $L/40$, so it is difficult to accurately
346 analyse the grid independence just by the waveform. A traditional decay rate parameter is adopted,
347 namely $\delta = (a_{probe} - a_{initial})/a_{initial}$, where $a_{initial}$ is the ISW amplitude value at the initial moment, a_{probe} is
348 the ISW amplitude value of the probe $10L$ away from the initial ISW. Fig. 4(b) shows the relationship
349 between the decay rate of the ISW amplitude and the grid quantity per unit length for different mesh
350 sizes. As shown in Fig. 4(b), the decay rate of the ISW amplitude tends to be smooth as the grid number



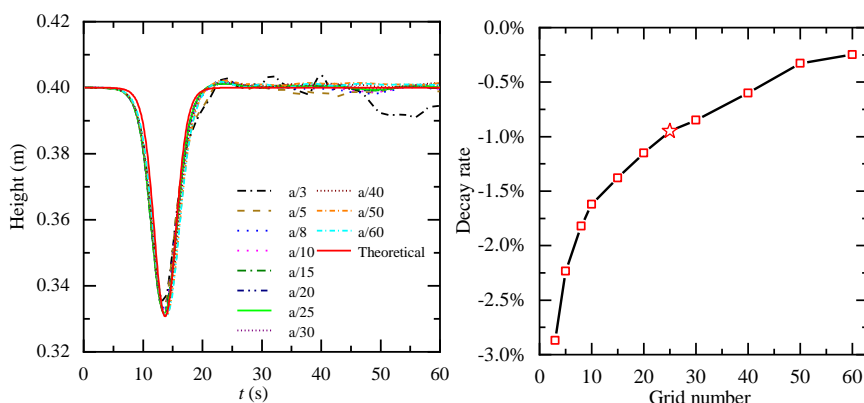
351 per unit length increases to 160 ($\Delta x = L/150$), and then the increase in the grid quantity has a relatively
352 small effect on the decay rate. Therefore, for ISWFoam developed in this paper, we suggest that the
353 dimensions of the horizontal grid are $L/150$.



354
355 Figure 4: Grid independence in the horizontal direction at probe P1: (a) comparison of waveform and (b) decay
356 rate.

357 3.2 Grid independence in the vertical direction

358 Second, we analyse the grid independence in the vertical direction, with a constant cell width of Δx
359 $= L/150$ m. Fig. 5 shows the results of a comparison of the waveform and decay rate of the ISW amplitude
360 in the vertical direction at probe P1 with the ISWFoam using a wide range of grid configurations. The
361 results also show a negligible difference in the waveform when the mesh size is less than $a/10$, so it is
362 difficult to accurately analyse the grid independence just by the waveform. As shown in Fig. 5(b), the
363 decay rate of the ISW amplitude decreases as the grid quantity increases in a wave height range before
364 the numerical oscillation occurs. Here, we assume that the grid size with the decay rate of the ISW
365 amplitude less than one percent is the appropriate vertical grid size; namely, the vertical grid size is $a/25$
366 m. Therefore, for ISWFoam developed in this paper, we suggest that the dimensions of the vertical grid
367 be $a/25$.



368
369 Figure 5: Grid independence analysis in the vertical direction at probe P1: (a) comparison of waveform and (b)
370 decay rate.

371 Finally, for ISWfoam developed in this paper, we suggest that the dimensions of the horizontal grid
372 are $L/150$, while the vertical grid is $a/25$.

373 4. Model verification and results

374 To verify the numerical model of the ISWs, the propagation of ISWs on a flat bottom section,
375 submerged triangular ridge and slopes is calculated, and the numerical results are compared with the
376 corresponding experimental results. To verify the correctness of Coriolis code implantation and reflect
377 the role of local mesh refinement, the propagation of ISWs on a flat bottom section of actual ocean scale
378 and a Gaussian ridge is calculated.

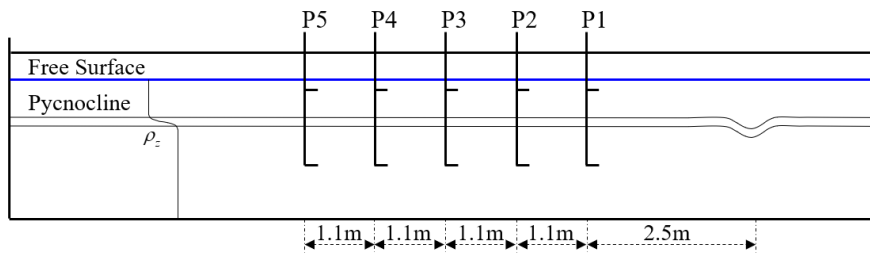
379 4.1 ISW propagating on a flat bottom section

380 4.1.1 Experimental data used

381 In this section, ISWfoam is verified by employing ISWs propagating on a flat bottom section with
382 Case Flat_4 in the continuously stratified laboratory experiment described in Hsieh et al. (2014). The
383 physical dimensions and ultrasonic probe locations in the experiments of Hsieh et al. (2014), as shown
384 in Fig. 6, are adopted to establish the numerical computation domain. We set up a numerical tank of the
385 experiment of Hsieh and co-authors, which includes a tank that is 15 m long, 0.5 m wide and has a stable
386 water depth of 0.5 m; the fluid densities of the upper (ρ_1) and lower (ρ_2) layers are 996 kg/m³ and 1030
387 kg/m³, respectively; the ISW amplitude (a) is 0.068 m; the location of the centre of the pycnocline (z_{pyc})
388 is 0.4 m, the pycnocline thickness (d_{pyc}) is 0.04 m vertically, and the depths of the upper (h_1) and lower



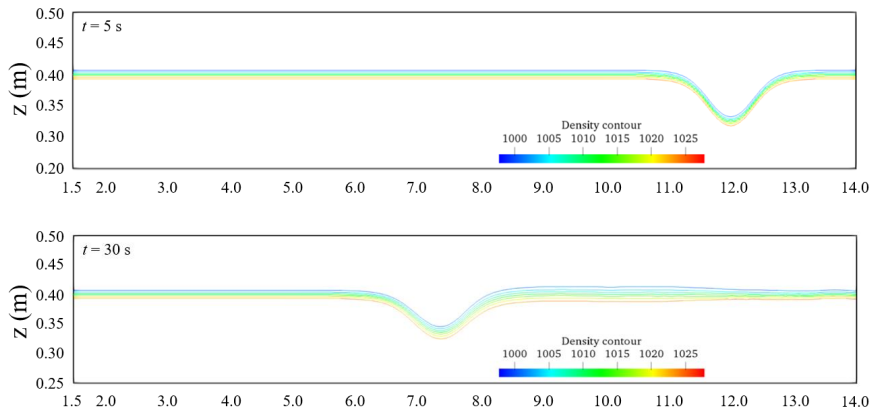
389 (h_2) layers are 0.1 m and 0.4 m, respectively. The grid is uniform in the x -direction, y -direction and z -
 390 direction, and the sizes are $\Delta x = 1.5 \times 10^{-2}$ m, $\Delta y = 1.5 \times 10^{-2}$ m and $\Delta z = 2.72 \times 10^{-3}$ m, respectively. The
 391 sponge layer on both sides, whose length is double wave characteristic length, has been checked to
 392 properly dissipate the reflected wave. Slip boundary conditions are applied to the bottom and both sides,
 393 while cyclic boundary conditions are assigned to the inlet and outlet boundaries. The top boundary is a
 394 rigid lid. The boundary conditions related to the density field are no-flux boundary conditions.



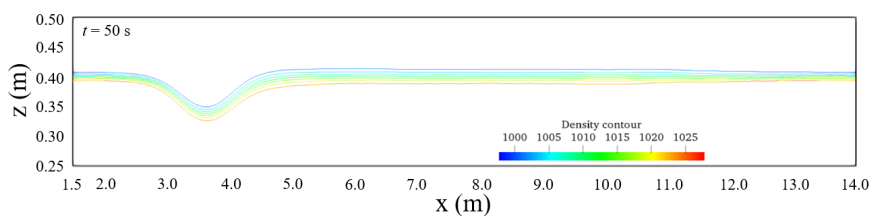
395
 396 Figure 6: Schematic diagram of probe position (P1–P5) (Hsieh et al. (2014)).

397 4.1.2 Comparisons between the numerical and experimental results

398 Fig. 7 shows the density contours at three different times from Case Flat_4 in the laboratory
 399 experiment of Hsieh and coworkers, showing the stable evolution of an ISW. The results also show the
 400 realistic evolution of the thickening of the pycnocline after ISW propagation because of convection and
 401 diffusion. At the same time, the propagation of the ISW is stable and unbroken.



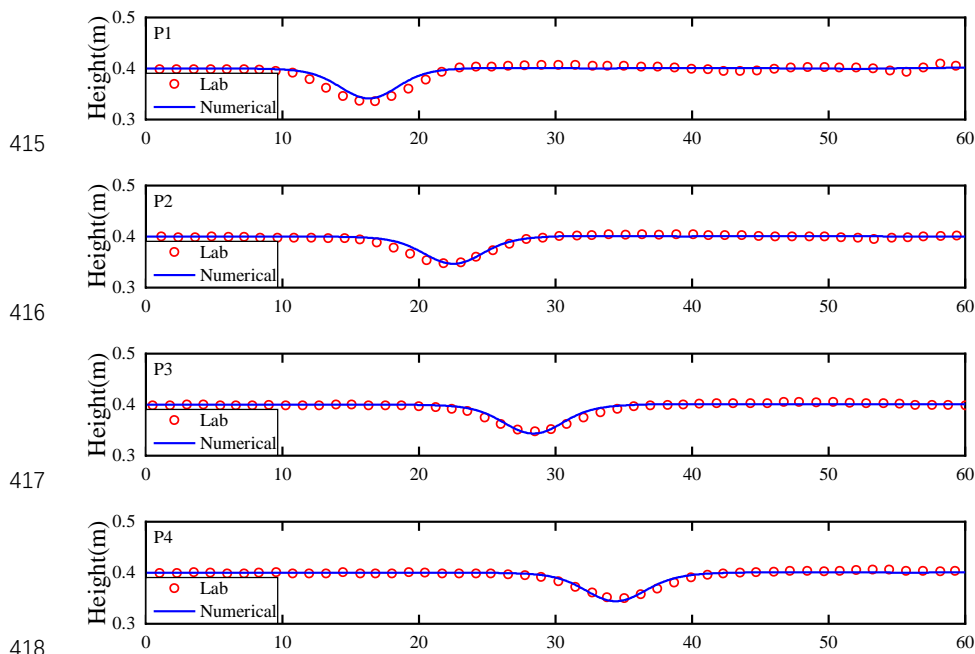
403



404
405

Figure 7: Density contours at different moments.

406 To further verify the model, the waveform is compared between the numerical simulations and the
407 experimental measurements, and the measurement point selection is the same as the experimental setting,
408 as shown in Fig. 6. Fig. 8 shows the comparison results between the waveform simulated by ISWFOam
409 and the experimental results at probes P1-P5. Fig. 8 shows that the results of the numerical simulations
410 agree with the experimental results (red circle). Notably, the laboratory wave height at the probe P1
411 measurement point is greater than the numerical simulation results, and the wave surface of the laboratory
412 wave is not smooth, which is caused by the wave generation method using the gravity collapse
413 mechanism in the laboratory. In general, the model developed in this paper can simulate the generation
414 and evolution of ISWs in continuously stratified fluids.

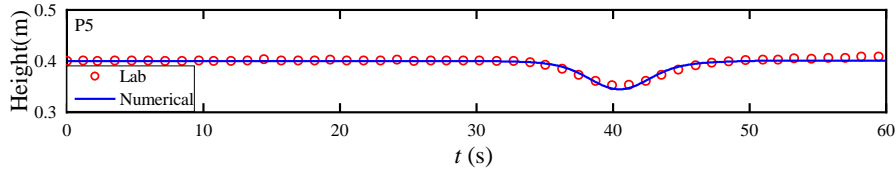


415

416

417

418



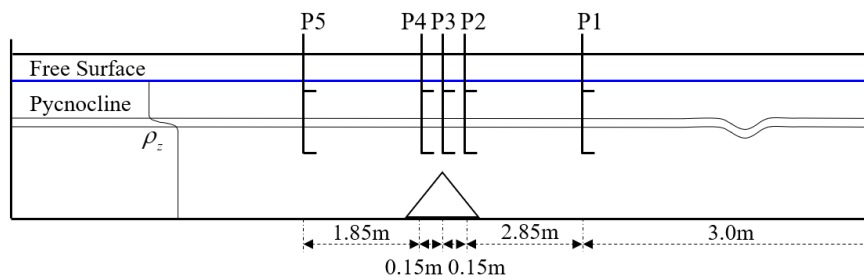
419

420 Figure 8: Comparison of the waveform between the experimental results and numerical simulation results at
 421 probes P1-P5.

422 **4.2 ISW propagating over a submerged triangular ridge**

423 **4.2.1 Experimental data used**

424 In this section, the validation of the numerical model is conducted through an ISW propagating over
 425 a submerged triangular ridge with the continuously stratified experiments described in [Hsieh et al. \(2015\)](#).
 426 The laboratory tank is 12 m long and has a stable water depth of 0.5 m, with which the fluid system has
 427 a finite thickness of the pycnocline. The specific experimental parameters used for validation of
 428 ISWfoam include the various depths of the upper (h_1) and lower (h_2) layers; the fluid density of the upper
 429 (ρ_1) and lower (ρ_2) layers of 996 kg/m^3 and 1030 kg/m^3 , respectively; the ISW amplitude ($\alpha = 0.056 \text{ m}$);
 430 the location of the centre of the pycnocline ($z_{pyc} = 0.4 \text{ m}$); the thickness of the pycnocline ($d_{pyc} = 0.04 \text{ m}$
 431 vertically); the height of the isosceles triangular ridge ($h_s = 0.30 \text{ m}$ vertically); and the slope angle of the
 432 ridge for $\alpha = 45^\circ$. The physical dimensions, and ultrasonic probe locations in the experiments of [Hsieh](#)
 433 [et al. \(2015\)](#), as shown in Fig. 9, are adopted to establish the numerical computation domain.



434

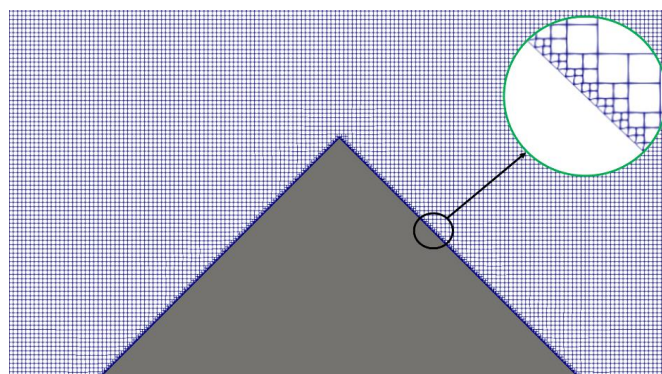
435 Figure 9: Schematic illustration of the laboratory setup and the locations of the probes ([Hsieh et al. \(2015\)](#)).

436 **4.2.2 Numerical implementation**

437 The numerical tank is designed to reproduce the experiment described in Fig. 9. The unstructured
 438 grid and local mesh refinement based on the finite volume method are used to construct the computational
 439 domain and discretize the governing equations. The grid is uniform in the x -direction, y -direction and z -



440 direction, and the sizes are $\Delta x = 2 \times 10^{-3}$ m, $\Delta y = 2 \times 10^{-3}$ m and $\Delta z = 2 \times 10^{-3}$ m, respectively. The precise
441 grid described triangular ridge section is $\Delta x = 2.5 \times 10^{-4}$ m, $\Delta y = 2.5 \times 10^{-4}$ m and $\Delta z = 2.5 \times 10^{-4}$ m at the
442 slope, as shown in Fig. 10. The sponge layer on both sides, whose length is double the wave characteristic
443 length defined through integration of the wave profile in Section 3 for this case, has been checked to
444 absorb the reflected wave well. A rigid wall conditions is applied to both sides, while the slip and slip
445 conditions are assigned to the bottom and the surface of the submerged ridge boundaries, respectively.
446 The top boundary is a rigid lid. The inlet and outlet boundaries adopt cyclic boundary condition. The
447 boundary conditions related to the density field are no-flux boundary conditions.

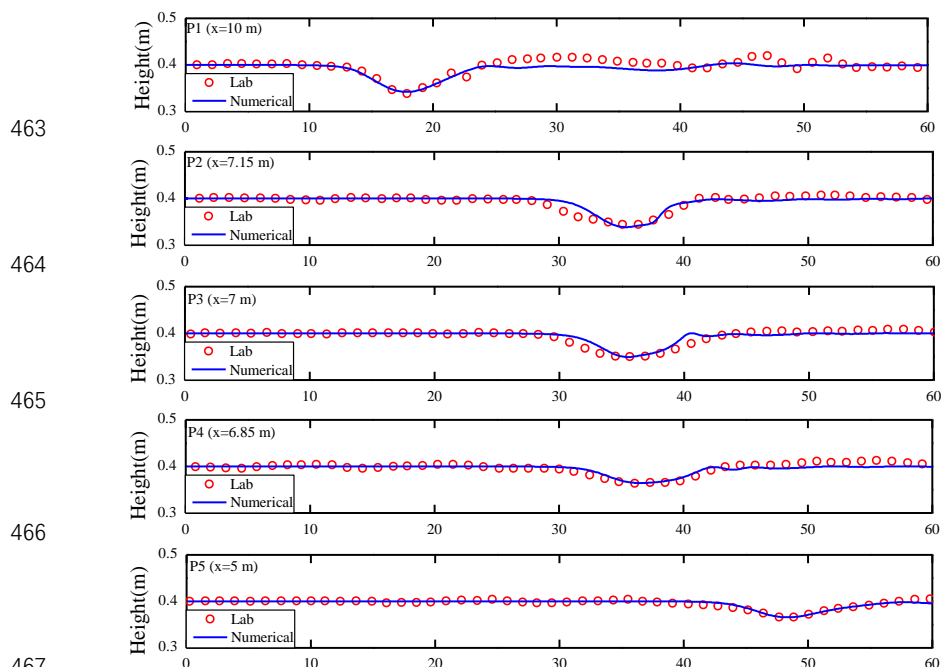


448
449

Fig. 10. Schematic of the mesh

4.2.3 Comparisons between the numerical and experimental results

451 Fig. 11 shows the comparison results between the waveform calculated by ISWFOam and the
452 experimental results at probes P1-P5. In each subplot, the results of the numerical simulations (blue line)
453 are found to be in good agreement with the experimental results (red circle). From Fig. 11 (a), the
454 numerical simulation result of the probe P1 measurement after 20 s is different from the experimental
455 results, which is caused by the different ISW generation methods. For the experimental results, the first
456 large leading ISW is formed via the gravity collapse mechanism, which is trailed by a train of small-
457 amplitude mode-one waves that is generated due to shear instabilities. However, the initialization method
458 used to generate an initial ISW for the numerical simulation in this paper is more stable than the gravity
459 collapse mechanism, so the rear part of the ISW is relatively flat compared to the experimental results
460 for probe P1. In Fig. 11, the waveform of the ISW gradually evolves towards a flat waveform due to the
461 interaction between the ISW and the ridge. In general, the model developed in this paper can simulate
462 the interaction between ISWs and structures.



463

464

465

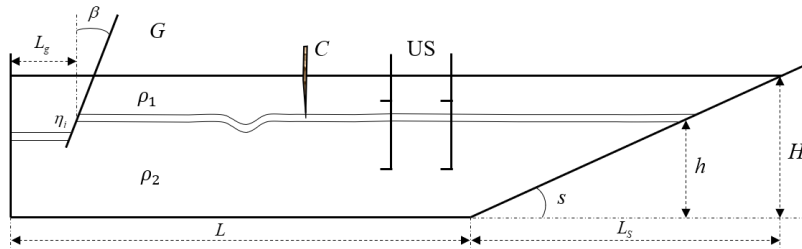
466

467

468 Figure 11: Comparison of the waveform between the experimental results in Hsieh et al. (2015) and numerical
469 simulation results at probes P1-P5.

470 4.3 ISW propagating on a slope

471 To verify the ability and accuracy of simulating the ISW breaking of the numerical model, two
472 continuously stratified laboratory experiments (12 and 15) of Michallet and Ivey. (1999) are chosen for
473 the simulation in this section. The experimental setup is represented schematically in Fig. 12. We set up
474 a numerical tank of the experiment of Michallet and Ivey. (1999), which includes a tank is $L=4.2$ m long,
475 0.25 m wide and has a water depth of 0.15 m. The layer thickness ratio (h/H) varies from 0.60–0.91. A
476 linear slope $s=0.214$ starts at 0.7 m from the right end of the tank for experiments 12 and 15. The grid
477 is uniform in the x -direction, y -direction and z -direction, and the sizes are $\Delta x=2.5\times 10^{-3}$ m, $\Delta y=2.5\times 10^{-3}$
478 m and $\Delta z=1.25\times 10^{-3}$ m, respectively. The precise grid describing the slope section is $\Delta x=\Delta y=6.25\times 10^{-4}$
479 m and $\Delta z=3.125\times 10^{-4}$ m at the slope.



480
 481 Figure 12: Schematic diagram of the laboratory setup. “C” and “US” represent the experimental device at probes.
 482 The sponge layer on the left side, whose length is the double wave characteristic length, is checked
 483 to properly dissipate the reflected wave. Slip boundary conditions are applied to the bottom and both
 484 sides, while slip boundary conditions are assigned to the top boundaries. The boundary conditions related
 485 to the density field are no-flux boundary conditions.

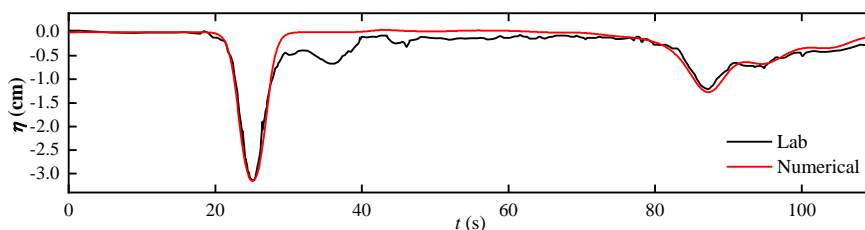
486 The vertical profile of the initial density is given by a hyperbolic tangent function profile

$$487 \quad \bar{\rho}(z) = \rho_1 + \frac{\Delta\rho}{2} \left\{ 1 + \tanh \left[\frac{-(z - z_{pyc})}{d_{pyc}} \right] \right\} \quad (44)$$

488 where z is the vertical position, $\rho_1 = 1 \times 10^3 \text{ kg/m}^3$ is the base density field, $\Delta\rho$ is the change in the density,
 489 z_{pyc} is the location of the centre of the pycnocline, and d_{pyc} is the thickness of the pycnocline.

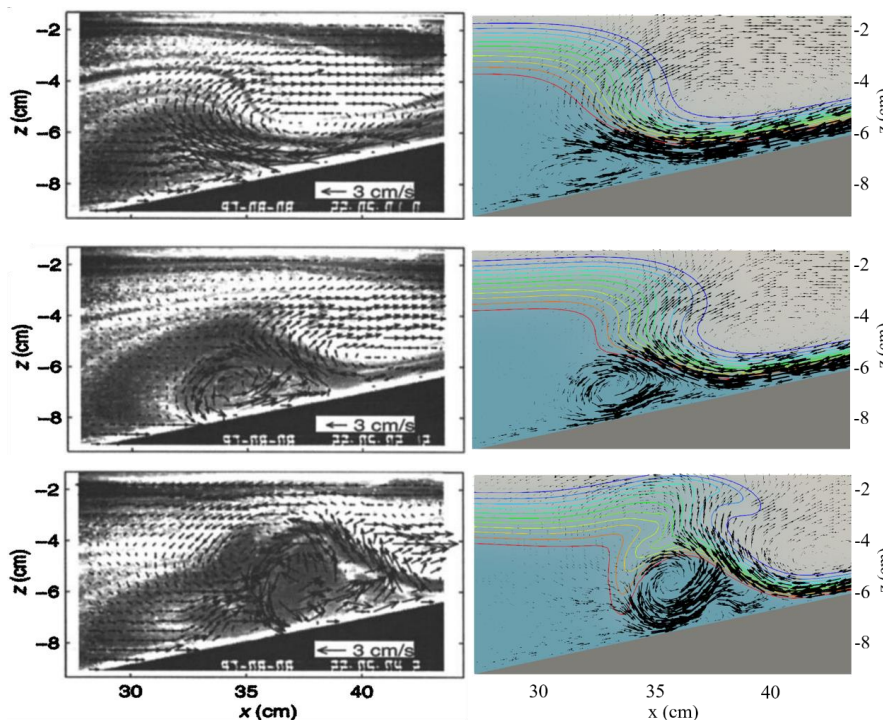
490 4.3.1 Case one and results

491 The first case of model verification is experiment 12 of Michallet and Ivey. (1999) in this section.
 492 The layer thickness ratio (h/H) is 0.84, and the density change ($\Delta\rho$) value is 14 kg/m^3 . Fig. 13 presents
 493 the time series for the interface displacement (ζ) for experiment 12 of Michallet and Ivey. (1999). The
 494 results indicate reasonably good agreement between the time series of the simulated interface
 495 displacement and that of the laboratory results. The first trough centred around $t = 25 \text{ s}$ represents the
 496 incident ISW propagating the probe 99.8 cm away from the start of the slope. The second trough centred
 497 at approximately $t = 87 \text{ s}$ represents the reflected ISW at the generation side, which has a smaller
 498 amplitude and a longer wavelength than the incident ISW as the energy in the wave decreases. As shown
 499 in Fig. 13, the smooth waveform of the incident ISW of the numerical simulation indicates that the
 500 initialization method of wave generation in this paper is more stable than the experiment.



501
502 Figure 13: Time series of the interface displacement. The probe was 99.8 cm away from the start of the slope.

503 Fig. 14 shows a comparison of ISWfoam results and the experimental observations of the velocity
504 field associated with the ISW run-up process along the slope. The model effectively reproduces
505 laboratory tests, such as the intensity and direction of the velocity field, the location of the vortices, and
506 the occurrence of boundary-layer separation beneath the ISW. Therefore, the model developed in this
507 paper can reflect the ISW breaking phenomenon during the propagation of ISWs along the slope.



510
511 Figure 14: Comparison of the velocity field between the experimental observation results in [Michallet and Ivey](#)
512 [\(1999\)](#) (left) and numerical simulation results (right).

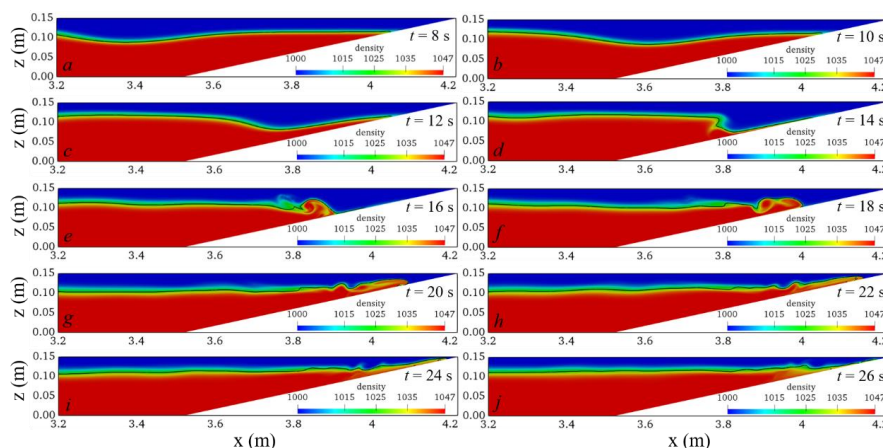
513 4.3.2 Case two and results

514 Another laboratory experiment that more clearly shows the ISW breaking phenomenon from



515 Experiment 15 of Michallet and Ivey. (1999) is used to verify the numerical model presented in this paper,
 516 and the corresponding numerical case is set corresponding to it. The layer thickness ratio (h/H) is 0.77,
 517 and the density change ($\Delta\rho$) value is 47 kg/m^3 . The wave amplitude and phase velocity at the slope
 518 calculated by ISWFoam are $2.71 \times 10^{-3} \text{ m}$ and $10.83 \times 10^{-1} \text{ m/s}$, which fit well with the experimental results
 519 of $2.7 \times 10^{-3} \text{ m}$ and $10.8 \times 10^{-1} \text{ m/s}$.

520 Fig. 15 shows the results of the numerical simulations of the ISWs propagating along the slope and
 521 wave breaking using ISWFoam. As the ISW propagates to the slope, according to the conservation of
 522 mass, the upper fluid forward and the downward velocity of the lower fluid increasing along the slope
 523 results in the formation of a thin boundary layer, as shown in Fig. 15(a), (b), and (c). At the same time,
 524 the amplitude of the ISW increases, and the rear of the ISW gradually becomes very steep but does not
 525 overturn. With the development of the ISW, the rear waveform of the ISW cannot maintain its stability
 526 and overturns forward, resulting in wave breaking, as shown in Fig. 15(d). After wave breaking occurs,
 527 the denser lower layer flow accelerates into the less dense upper layer flow, forming a mixture region,
 528 shown in Fig. 15(e). After the lower layer flow is drawn downward from beneath the ISW, a mixing
 529 region comprised of vortices is pushed upwards along the slope while the leading waveform is reflected,
 530 as shown in Fig. 15(f), (g), and (h). Fig. 15(i), (j) shows the falling process of ISWs. From the perspective
 531 of the entire process of wave breaking, the steepening of the rear waveform in this case is the main reason
 532 for wave breaking.



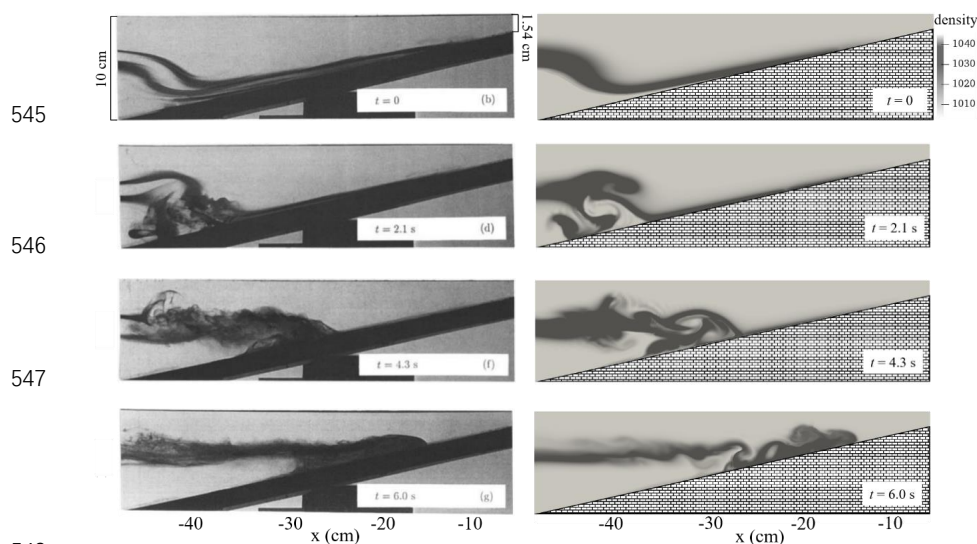
533
 534 Figure 15: Temporal and spatial variations in the ISWs breaking calculated using ISWFoam (the black line
 535 represents the waveform).

536 For comparison with the flow visualization image of the experiment, a specified thickness of the



537 pycnocline is presented, and the pycnocline ranges from 1003 kg/m^3 to 1045 kg/m^3 with dark colours as
538 shown in Fig. 16.

539 Fig. 16 compares the ISWfoam results and the experimental results of Michallet and Ivey. (1999)
540 before, during, and after ISW breaking. The results indicate that some main features of the laboratory
541 tests are reasonably well reproduced by ISWfoam, such as the profile of ISW, the location of the wave
542 breaking point, ISW arrival time, and spatial and temporal changes in the mixture region. Therefore, the
543 model developed in this paper can accurately simulate the ISW breaking phenomenon during the
544 propagation of ISWs along the slope.



548
549 Figure 16: Comparison of the density fields between the experimental observation results in Michallet and Ivey.
550 (1999) (left) and the numerical simulation results (right).

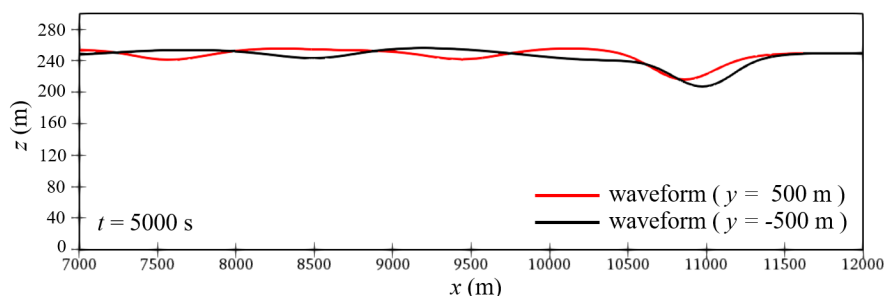
551 4.4 Coriolis force analysis

552 Notably, the previous verifications are all laboratory-scale verifications, thus, it is difficult to clearly
553 see the influence of the Coriolis force on ISWs. To verify the correctness of the Coriolis force added in
554 the code, we set up a 3D numerical tank, which includes a tank that is 15 km long, 1 km wide (y direction
555 from -500 m to 500 m) and has a water depth of 300 m . The depths of the upper (h_1) and lower (h_2) layers
556 are 50 m and 250 m , respectively, the densities of the upper and lower layers are 1022 kg/m^3 and 1028
557 kg/m^3 , respectively, the location of the centre of the pycnocline (z_{pyc}) is 250 m vertically, and the
558 pycnocline thickness (d_{pyc}) is 5 m vertically, the ISW amplitude (a) is 40 m . The grid gradually changes



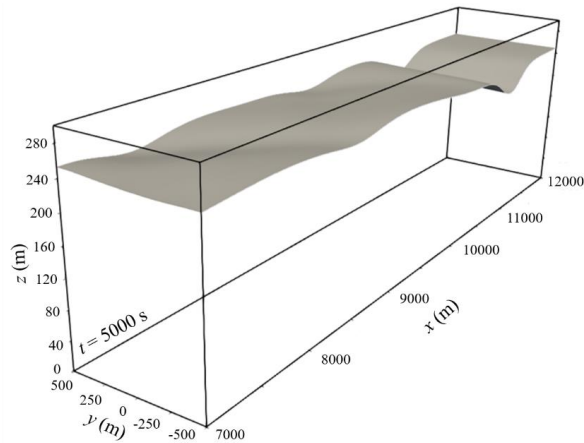
559 from $\Delta x = 100$ m to $\Delta x = 10$ m in the x -direction, the grids in the y -direction are uniform with a constant
560 cell width of $\Delta y = 10$ m, and the grids in the z -direction are non-uniform, with a minimum cell height of
561 $\Delta z = 2.5$ m near the interface of the ISW. To see the influence of the Coriolis force more clearly, the
562 Coriolis force parameter (Ω) is expanded 5 times, to $3.65 \times 10^{-4} \text{ s}^{-1}$. The sponge layer on both sides, whose
563 length is the double wave characteristic length, has been checked to properly dissipate the reflected wave.
564 Slip boundary conditions are applied to the bottom and both sides, while cyclic boundary conditions are
565 assigned to the inlet and outlet boundaries. The top boundary is a rigid lid. The boundary conditions
566 related to the density field are no-flux boundary conditions.

567 Figs 17 and 18 show the two-dimensional (2D) and three-dimensional (3D) waveform diagrams
568 when the ISW propagates for 5000s. The figures show that under the influence of the Coriolis force,
569 asymmetry is caused in the front and back wave surfaces, and the height difference is approximately 6
570 m. Since this summary only verifies the correctness of the Coriolis force implanted in the code, there is
571 no further quantitative analysis of the influence of the Coriolis force on ISWs. In general, ISWFoam can
572 effectively reflect the influence of the Coriolis force. At the same time, the influence of the Coriolis force
573 cannot be ignored when performing large-scale simulations.



574
575

Figure 17: Schematic of the waveforms on the front ($y = -500$) and back ($y = 500$).



576
577

Figure 18: Schematic of the three-dimensional waveform.

578 4.5 ISW propagating over a 3D Gaussian ridge

579 The ISWFoam model with unstructured grids and local mesh refinement can accurately simulate
580 the interaction between ISWs and complex structures and topography. However, the terrain in the
581 previous cases is relatively simple, and it is difficult to see such characteristics. Therefore, we designed
582 a case of an ISW propagating over a 3D Gaussian ridge. The 3D Gaussian ridge is obtained by rotating
583 a 2D Gaussian ridge

$$584 \quad z = ae^{-(x/l)^2} \quad (45)$$

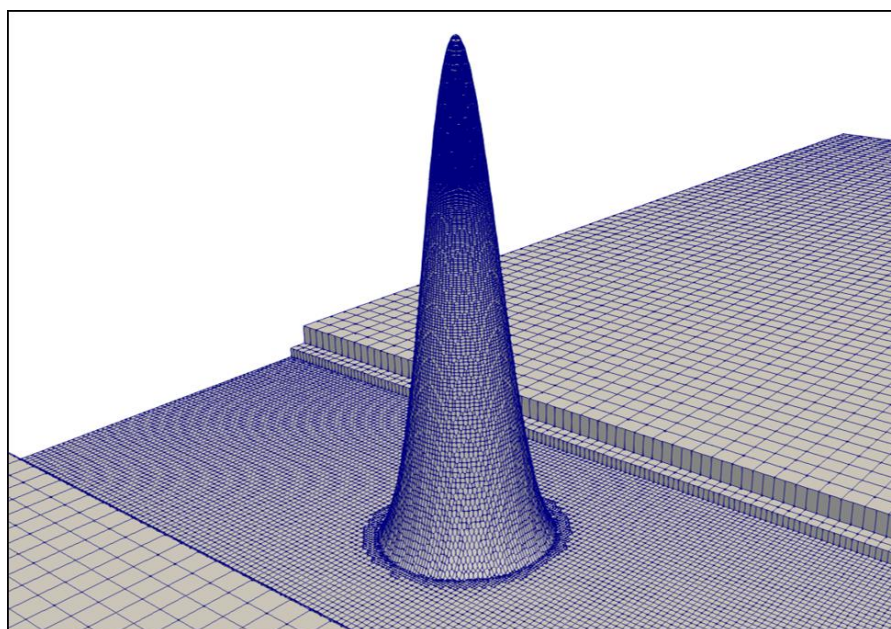
585 where a is the ridge amplitude, and l is the standard deviation.

586 With $a = 5$ m and $l = 0.5$, we can obtain a 2D Gaussian ridge with a height of 5 m and a bottom width of
587 2 m. Subsequently, the 3D Gaussian ridge can be obtained after a vertical rotation of 180 degrees.

588 We set up a 3D numerical tank, which includes a tank that is 150 m long, 20 m wide (y -direction
589 from -10 m to 10 m) and has a water depth of 6 m. The depths of the upper (h_1) and lower (h_2) layers are
590 1 m and 5 m, respectively, the densities of the upper and lower layers are 1000 kg/m^3 and 1030 kg/m^3 ,
591 respectively, the location of the centre of the pycnocline (z_{pyc}) is 5 m, and the pycnocline thickness (d_{pyc})
592 is 0.1 m vertically, the ISW amplitude (a) is 1 m. The Gaussian ridge is located at 80 m horizontally. The
593 grid is gradually changed from $\Delta x = 5$ m to $\Delta x = 0.2$ m in the x -direction, the grids in the y -direction are
594 uniform with a constant cell width of $\Delta y = 0.2$ m, and the grids in the z -direction are non-uniform, with
595 a minimum cell height of $\Delta z = 0.05$ m near the interface of the ISW. The precise grid described the 3D

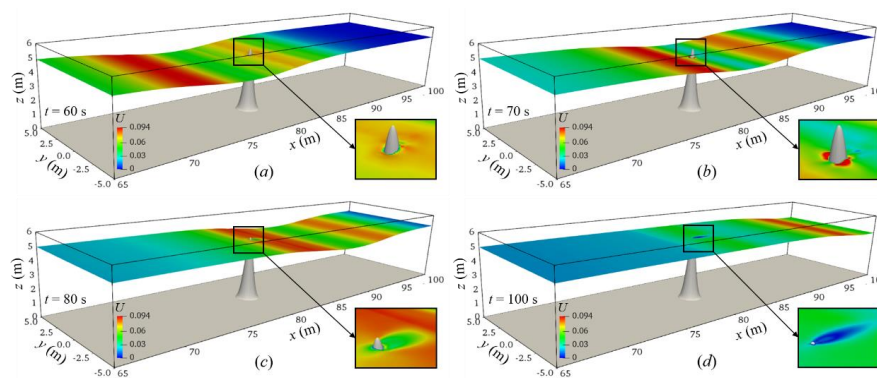


596 Gaussian ridge section as $\Delta x = 1.25 \times 10^{-2}$ m, $\Delta y = 1.25 \times 10^{-2}$ m and $\Delta z = 6.25 \times 10^{-3}$ m, as shown in Fig 19.
597 The sponge layer on both sides, whose length is the double wave characteristic length, has been checked
598 to properly dissipate the reflected wave. Slip boundary conditions are applied to the bottom and both
599 sides, while cyclic boundary conditions are assigned to the inlet and outlet boundaries. The top boundary
600 is a rigid lid. The boundary conditions related to the density field are no-flux boundary conditions.



601
602 Figure 19: Schematic of the local refinement of the grid.

603 Fig. 20. shows the temporal and spatial variations in the ISWs propagating over a 3D Gaussian
604 ridge. The ISW reaches the Gaussian ridge, causing the wave surface in front of the ridge to decrease,
605 and the wave surface behind the ridge to climb up the ridge, as shown in Fig. 20(a). Due to being
606 obstructed by the Gaussian ridge, flow around a ridge and wave surface uplift are generated on both sides
607 of the Gaussian ridge (perpendicular to the direction of wave propagation), as shown in Fig. 20(b). As
608 the ISW propagated over the Gaussian ridge, the wave surface climbed along the ridge, and at the same
609 time, low velocity was generated behind the ridge, as shown in Fig. 20(c). Since the top of the ridge is in
610 the pycnocline, there will be a low velocity area behind the ridge for a period of time after the ISW passes,
611 as shown in Fig. 20(d). In general, the ISWfoam model with unstructured grids and local mesh
612 refinement can simulate the interaction between ISWs and complex structures and topography.



613
614

Figure 20: Temporal and spatial variation in the ISWs propagating over a 3D Gaussian ridge.

615 5. Conclusions

616 In this paper, a numerical model referred to as ISWfoam with a modified $k-\omega$ SST model,
617 established by combining the density transport equation with a fully three-dimensional (3D) Navier-
618 Stokes equation, is developed to simulate ISWs in continuously stratified, incompressible, viscous fluids
619 based on the finite volume method with unstructured grids and local mesh refinement of OpenFOAM.
620 ISWfoam provides two initial wave generation methods to generate an ISW in continuously stratified
621 fluids, including solving the weakly nonlinear models of the eKdV equation and the fully nonlinear
622 models of the DJL equation. The verification process presents several applications, such as ISWs
623 propagating on flat bottoms including laboratory scale and actual ocean scale, and ISWs over a
624 submerged triangular ridge, a Gaussian ridge and slopes. The following conclusions were obtained as a
625 result of this study.

626 ISWfoam using the finite volume method with unstructured grids and local mesh refinement can
627 accurately simulate the generation and evolution of ISWs, the ISW breaking phenomenon and the
628 interaction between ISWs and complex structures and topography. The method of initializing the ISW
629 using weakly nonlinear eKdV equation models requires a period of movement before the jump of the
630 velocity field develops into a field with continuous changes in velocity. The DJL equation wave
631 generation method that considers the vertical velocity and the horizontal velocity along the vertical
632 gradient is better than the eKdV equation wave generation method that only provides the horizontal
633 average velocity. Using ISWfoam to simulate an ISW with infinite wave length, the metric for the
634 appropriate mesh size is given as follows: the dimensions of the horizontal grid are one-one hundred and



635 fiftieth of the characteristic length, while the vertical grid takes one-twenty fifth of the ISW amplitude.

636

637 **Computer code availability**

638 The ISWfoam code developed in this article can be downloaded for free from

639 <https://github.com/Mr-trekking/ISW.git>.

640 **Author contributions**

641 QZ and JL jointly developed this numerical method to calculate internal solitary waves in
642 continuously stratified fluids. JL developed the code. TC performed the computations. QZ and JL
643 jointly analysed the calculation results and wrote the paper together.

644 **Competing interest**

645 The authors of this paper declare that they have no conflicts of interest.

646 **Financial support**

647 This work is supported by grants from the National Key Research and Development Program of
648 China (2017YFC1404200), and the National Natural Science Foundation of China (51509183).

649 **Reference**

- Alford, M. H., Lien, R. C., Simmons, H., Klymak, J., Ramp, S., Yang, Y. J., Tang, D., and Chang, M. H.:
Speed and evolution of nonlinear internal waves transiting the South China Sea, *Journal of Physical
Oceanography*, 40, 1338-1355, doi:10.1175/2010JPO4388.1, 2010.
- Alford, M. H., MacKinnon, J. A., Nash, J. D., Simmons, H., Pickering, A., Klymak, J. M., Beitzel, T.:
Energy flux and dissipation in Luzon Strait: Two tales of two ridges, *Journal of Physical
Oceanography*, 41, 2211-2222. doi:10.1175/JPOD11073.1, 2011.
- Alford, M. H., Peacock, T., MacKinnon, J. A., Nash, J. D., Buijsman, M. C., Centurioni, L. R., Fu, K. H.:
The formation and fate of internal waves in the South China Sea, *Nature*, 521, 65-69,
doi:10.1038/nature14399, 2015.
- Aghsaee, P., Boegman, L., Lamb, K. G.: Breaking of shoaling internal solitary waves, *Journal of Fluid
Mechanics*, 659, 289. doi:10.1017/S002211201000248X, 2010.
- Aghsaee, P., Boegman, L., Diamessis, P. J., Lamb, K. G.: Boundary-layer-separation-driven vortex
shedding beneath internal solitary waves of depression, *Journal of Fluid Mechanics*, 690, 321,



- doi:10.1017/jfm.2011.432, 2012.
- Apel, J., Ostrovsky, L., Stepanyants, Y., Lynch, J.F.: Internal Solitons in the Ocean, Technical Report Woods Hole Oceanographic Institution., doi:10.1575/1912/1070, 2006.
- Bardina, J.E., Coakley, T.J., and Huang, P.G.: Turbulence Modeling Validation, Testing, and Development, NASA TM 110446, NASA Ames Research Center, Moffett Field, Calif. doi: 10.2514/6.1997-2121, 1997.
- Bell, J. B. and Marcus, D. L.: A second-order projection method for variable-density flows, *Journal of Computational Physics.*, 101(2), 334-348, doi:10.1016/0021-9991(92)90011-M, 1992.
- Brown, D. J. and Christie, D. R.: Fully nonlinear solitary waves in continuously stratified incompressible Boussinesq fluids, *Physics of Fluids.*, 10(10), 2569-2586, doi:10.1063/1.869771, 1998.
- Boegman, L. and Stastna, M.: Sediment resuspension and transport by internal solitary waves, *Annual review of fluid mechanics.*, 51, 129-154, doi:10.1146/annurev-fluid-122316-045049, 2019.
- Buijsman, M. C., McWilliams, J. C., and Jackson, C. R.: East-west asymmetry in nonlinear internal waves from Luzon Strait, *Journal of Geophysical Research: Oceans.*, 115(C10), doi:10.1029/2009JC006004, 2010.
- Cai, S., Xie, J., and He, J.: An overview of internal solitary waves in the South China Sea, *Surveys in Geophysics.*, 33, 927-943, doi:10.1007/s10712-012-9176-0, 2012.
- Cheng, M. H., Hwang, R. R., and Hsieh, C. M.: Numerical study on the transformation of an internal solitary wave propagating across a vertical cylinder, *Applied Ocean Research.*, 95, 102016, doi:10.1016/j.apor.2019.102016, 2020.
- Choi, W. and Camassa, R.: Fully nonlinear internal waves in a two-fluid system, *Journal of Fluid Mechanics.*, 396, 1-36, doi:10.1017/S0022112099005820, 1999
- Deshpande, S. S., Anumolu, L., and Trujillo, M. F.: Evaluating the performance of the two-phase flow solver interFoam, *Computational Science. Discovery* 5, 014016, 1-36, doi:10.1088/1749-4699/5/1/014016, 2012.
- Diamessis, P. J., Domaradzki, J. A., and Hesthaven, J. S.: A spectral multidomain penalty method model for the simulation of high Reynolds number localized incompressible stratified turbulence, *Journal of Computational Physics.*, 202(1), 298-322, doi:10.1016/j.jcp.2004.07.007, 2005.
- Ding, W., Ai, C., Jin, S., Lin, J.: Numerical investigation of an internal solitary wave interaction with horizontal cylinders, *Ocean Engineering.*, 208, 107430, doi:10.1016/j.oceaneng.2020.107430, 2020.
- Dunphy, M., Subich, C., and Stastna, M.: Spectral methods for internal waves: indistinguishable density profiles and double-humped solitary waves, *Nonlinear Processes in Geophysics.*, 18(3), 351-358, doi:10.5194/npg-18-351-2011, 2011.
- Farmer, D. M. and Smith, J. D.: Tidal interaction of stratified flow with a sill in Knight Inlet, *Deep Sea Research Part A. Oceanographic Research Papers.*, 27(3-4), 239-254, doi:10.1016/0198-0149(80)90015-1, 1980.
- Fringer, O. B., Gerritsen, M., and Street, R. L.: An unstructured-grid, finite-volume, nonhydrostatic, parallel coastal ocean simulator, *Ocean Modelling.*, 14(3-4), 139-173,



- doi:10.1016/j.ocemod.2006.03.006, 2006.
- Fu, D. M., You, Y. X., and Li, W., Numerical simulation of internal solitary waves with a submerged body in a two-layer fluid, *Ocean Engineering (Haiyang Gongcheng)*, 37(3), 38-44, 2009.
- Gao, X. Y., You, Y. X., Wang, X., Li, W.: Numerical simulation for the internal solitary wave based on MCC theory, *Ocean Engineering (Haiyang Gongcheng)*, 30(4), 29-36, 2012.
- Grimshaw, R., Pelinovsky, E., Talipova, T., Kurkina, O.: Internal solitary waves: propagation, deformation and disintegration, *Nonlinear Processes in Geophysics*, 17(6), 633-649, doi:10.5194/npg-17-633-2010, 2010.
- Guo, C. and Chen, X.: A review of internal solitary wave dynamics in the northern South China Sea, *Progress in Oceanography*, 121, 7-23, doi:10.1016/j.pocean.2013.04.002, 2014.
- Hallberg, R. and Rhines, P.: Buoyancy-driven circulation in an ocean basin with isopycnals intersecting the sloping boundary, *Journal of Physical Oceanography*, 26(6), 913-940, doi:10.1175/1520-0485(1996)026<0913:BDCIAO>2.0.CO;2, 1996.
- Hallberg, R.: Stable split time stepping schemes for large-scale ocean modeling, *Journal of Computational Physics*, 135(1), 54-65, doi:10.1006/jcph.1997.5734, 1997.
- Helfrich, K. R. and Melville, W. K.: Long nonlinear internal waves, *Annu. Rev. Fluid Mech.*, 38, 395-425, doi:10.1146/annurev.fluid.38.050304.092129, 2006.
- Hsieh, C. M., Hwang, R. R., Hsu, J. R. C., Cheng, M. H.: Flow evolution of an internal solitary wave generated by gravity collapse, *Applied Ocean Research*, 48, 277-291, doi:10.1016/j.apor.2014.10.001, 2014.
- Hsieh, C. M., Hwang, R. R., Hsu, J. R. C., Cheng, M. H.: Numerical modeling of flow evolution for an internal solitary wave propagating over a submerged ridge, *Wave Motion*, 55, 48-72, doi:10.1016/j.wavemoti.2014.12.008, 2015.
- Hibiya, T.: The generation of internal waves by tidal flow over Stellwagen Bank, *Journal of Geophysical Research: Oceans*, 93, 533-542, doi:10.1029/JC093iC01p00533, 1988.
- Hu, H. C., Tong, B. and Lou, S. Y.: Nonsingular positon and complexiton solutions for the coupled KdV system, *Physics Letters A*, 351, 403-412, doi:10.1016/j.physleta.2005.11.047, 2006.
- Huthnance, J. M.: Waves and currents near the continental shelf edge, *Progress in Oceanography*, 10, 193-226, doi:10.1016/0079-6611(81)90004-5, 1981.
- Issa, R. I.: Solution of the implicitly discretised fluid flow equations by operator-splitting, *Journal of computational physics*, 62(1), 40-65, doi:10.1016/0021-9991(86)90099-9, 1986.
- Jasak, H.: Error Analysis and Estimation for the Finite Volume Method with Applications to Fluid Flows, Ph.D. thesis. Imperial College London, 1996.
- Ko, D. S., Martin, P. J., Rowley, C. D., Preller, R. H.: A real-time coastal ocean prediction experiment for MREA04, *Journal of Marine Systems*, 69(1-2), 17-28, doi:10.1016/j.jmarsys.2007.02.022, 2008.
- Kubota, T., Ko, D. R. S., and Dobbs, L. D.: Weakly-nonlinear, long internal gravity waves in stratified fluids of finite depth, *Journal of Hydronautics*, 12, 157-165, doi:10.2514/3.63127, 1978.



- Lamb, K. G.: Numerical experiments of internal wave generation by strong tidal flow across a finite amplitude bank edge, *Journal of Geophysical Research: Oceans.*, 99, 843-864, doi:10.1029/93JC02514, 1994.
- Lamb, K. G. and Yan, L.: The evolution of internal wave undular bores: comparisons of a fully nonlinear numerical model with weakly nonlinear theory, *Journal of physical oceanography.*, 26(12), 2712-2734, doi:10.1175/1520-0485(1996)026<2712:TEOIWU>2.0.CO;2, 1996.
- Lamb, K. G. and Nguyen, V. T.: Calculating energy flux in internal solitary waves with an application to reflectance, *Journal of Physical Oceanography.*, 39, 559-580, doi:10.1175/2008JPO3882.1, 2009.
- Lamb, K. G.: Energy and pseudoenergy flux in the internal wave field generated by tidal flow over topography, *Continental Shelf Research.*, 27, 1208-1232, doi:10.1016/j.csr.2007.01.020, 2007.
- Li, J. Y., Zhang, Q. H., and Chen. T. Q.: Numerical Simulation of Internal Solitary Wave in Continuously Stratified Fluid, *Journal of Tianjin University (Science and Technology).*, 54(02), 161-170, DOI:10.11784/tdxbz202001025, 2021.
- Li, Q. and Farmer, D. M.: The generation and evolution of nonlinear internal waves in the deep basin of the South China Sea, *Journal of Physical Oceanography.*, 41(7), 1345-1363, doi:10.1175/2011JPO4587.1, 2011.
- Li, Z., You, Y. U., Zhe, S., Zang, J. M., LI, Z. H., Yu, Z. B.: CFD Simulation of Internal Solitary Wave Using the Volume-of-fluid Method within OpenFOAM, *DEStech Transactions on Computer Science and Engineering*, doi:10.12783/dtsc/mmsta2017/19617, 2017 (mmsta).
- Long, R. R.: Some aspects of the flow of stratified fluids: I. A theoretical investigation, *Tellus.*, 5(1), 42-58, doi:10.3402/tellusa.v5i1.8563, 1953.
- Lou, S. Y., Tong, B., Hu, H. C., Tang, X. Y.: Coupled KdV equations derived from two-layer fluids, *Journal of Physics A: Mathematical and General.*, 39, 513, doi:10.1088/0305-4470/39/3/005, 2005.
- Meng, Q. and Zhang, C.: A third-order KdV solution for internal solitary waves and its application in the numerical wave tank, *Journal of Ocean Engineering and Science.*, 1(2), 93-108, doi:10.1016/j.joes.2016.03.002, 2016.
- Menter, F. R., Kuntz, M., and Langtry, R.: Ten years of industrial experience with the SST turbulence model, *Turbulence, heat and mass transfer.*, 4(1), 625-632, 2003.
- Michallet, H. and Ivey, G. N.: Experiments on mixing due to internal solitary waves breaking on uniform slopes, *Journal of Geophysical Research: Oceans.*, 104, 13467-13477, doi:10.1029/1999JC900037, 1999.
- Miyata, M.: An internal solitary wave of large amplitude, *La Mer.* 23, 43-48, 1985.
- Miyata, M.: Long Internal Waves of Large Amplitude. Springer, Berlin, pp. 399-406. doi:10.1007/978-3-642-83331-1_44. 1988.
- OpenFOAM User Guide 2019 <http://www.openfoam:docs/>.
- OpenFOAM User Guide 2019 <http://www.openfoam.com/documentation/user-guide>.
- Osborne, A. R. and Burch, T. L.: Internal solitons in the Andaman Sea, *Science.*, 208, 451-460, doi:10.1126/science.208.4443.451, 1980.



- Rayson, M. D., Ivey, G. N., Jones, N. L., Fringer, O. B.: Resolving high-frequency internal waves generated at an isolated coral atoll using an unstructured grid ocean model, *Ocean Modelling.*, 122, 67-84, doi:10.1016/j.ocemod.2017.12.007, 2018.
- Sandstrom, H. and Elliott, J. A.: Internal tide and solitons on the Scotian Shelf: A nutrient pump at work, *Journal of Geophysical Research: Oceans.*, 89, 6415-6426, doi:10.1029/JC089iC04p06415, 1984.
- Seadawy, A. R.: Exact solutions of a two-dimensional nonlinear Schrödinger equation, *Applied Mathematics Letters.*, 25, 687-691, doi:10.1016/j.aml.2011.09.030, 2012.
- Seadawy, A. R., Lu, D., and Yue, C.: Travelling wave solutions of the generalized nonlinear fifth-order KdV water wave equations and its stability, *Journal of Taibah University for Science.*, 11, 623-633, doi:10.1016/j.jtusci.2016.06.002, 2017.
- Shaw, P. T., Ko, D. S., and Chao, S. Y.: Internal solitary waves induced by flow over a ridge: With applications to the northern South China Sea, *Journal of Geophysical Research: Oceans.*, 114(C2), doi:10.1029/2008JC005007, 2009.
- Simmons, H. L., Hallberg, R. W., and Arbic, B. K.: Internal wave generation in a global baroclinic tide model, *Deep Sea Research Part II: Topical Studies in Oceanography.*, 51(25-26), 3043-3068, doi:10.1016/j.dsr2.2004.09.015, 2004.
- Smedstad, O. M., Hurlburt, H. E., Metzger, E. J., Rhodes, R. C., Shriver, J. F., Wallcraft, A. J., Kara, A. B.: An operational eddy resolving 1/16 global ocean nowcast/forecast system, *Journal of Marine Systems.*, 40, 341-361, doi:10.1016/S0924-7963(03)00024-1, 2003.
- Subich, C. J., Lamb, K. G., and Stastna, M.: Simulation of the Navier–Stokes equations in three dimensions with a spectral collocation method, *International Journal for Numerical Methods in Fluids.*, 73(2), 103-129, doi:10.1002/flid.3788, 2013.
- Thiem, Ø., Carr, M., Berntsen, J., Davies, P. A.: Numerical simulation of internal solitary wave-induced reverse flow and associated vortices in a shallow, two-layer fluid benthic boundary layer. *Ocean dynamics.*, 61, 857, doi:10.1007/s10236-011-0396-5, 2011.
- Turkington, B., Eydeland, A., and Wang, S.: A computational method for solitary internal waves in a continuously stratified fluid, *Studies in Applied Mathematics.*, 85, 93-127, doi:10.1002/sapm199185293, 1991.
- Vlasenko, V., Stashchuk, N., and Hutter, K.: *Baroclinic Tides: Theoretical Modeling and Observational Evidence*, Cambridge University Press., doi:10.5670/oceanog.2006.107, 2005.
- Vlasenko, V., Stashchuk, N., Guo, C., Chen, X.: Multimodal structure of baroclinic tides in the South China Sea, *Nonlinear Processes in Geophysics.*, 17(5), 529-543, doi:10.5194/npg-17-529-2010, 2010.
- Wang, X., Zhou, J. F., Wang, Z., You, Y. X.: A numerical and experimental study of internal solitary wave loads on semi-submersible platforms, *Ocean Engineering.*, 150, 298-308, doi:10.1016/j.oceaneng.2017.12.042, 2018.
- Wei, G., Du, H., Xu, X. H., Zhang, Y. M., Qu, Z. Y., Hu, T. Q., You, Y. X.: Experimental investigation of the generation of large-amplitude internal solitary wave and its interaction with a submerged slender



- body, *Science China Physics, Mechanics and Astronomy.*, 57, 301-310, doi:10.1007/s11433-013-5196-0, 2014.
- Wilcox, D. C.: Comparison of two-equation turbulence models for boundary layers with pressure gradient, *AIAA journal.*, 31(8), 1414-1421, doi:10.2514/3.11790, 1993.
- Xu, C. and Stastna, M.: Instability and cross-boundary-layer transport by shoaling internal waves over realistic slopes, *Journal of Fluid Mechanics.*, 895, doi:10.1017/jfm.2020.389, 2020.
- Yuan, G. and Xiao-Yan, T.: A coupled variable coefficient modified KdV equation arising from a two-layer fluid system, *Communications in Theoretical Physics.*, 48, 961-970, doi:10.1088/0253-6102/48/6/001, 2007.
- Zhang, Z., Fringer, O. B., and Ramp, S. R.: Three-dimensional, nonhydrostatic numerical simulation of nonlinear internal wave generation and propagation in the South China Sea, *Journal of Geophysical Research: Oceans.*, 116(C5), doi:10.1029/2010JC006424, 2011.
- Zhang, H. G., Gu J. B., Jia, H. Q., Gu, B.: A numerical model for internal wave propagation in continuously stratified ocean, *Chinese Journal of Theoretical and Applied Mechanics.*, 44, 896-903, doi:10.6052/0459-1879-12-195, 2012.